Thesis for the degree of Doctor of Philosophy

Tracing cosmic magnetic fields using molecules

BOY LANKHAAR

Astronomy and Plasma Physics
Department of Space, Earth and Environment
CHALMERS UNIVERSITY OF TECHNOLOGY
Gothenburg, Sweden 2021

Tracing cosmic magnetic fields using molecules
BOY LANKHAAR

ISBN: 978-91-7905-445-8

Doktorsavhandlingar vid Chalmers tekniska högskola
Ny serie Nr 4912
ISSN0346-718X

Division of Astronomy & Plasma Physics
Department of Space, Earth and Environment
Chalmers University of Technology
SE–412 96 Gothenburg, Sweden
Phone: +46 (0)31–772 1000

Contact information:
Boy Lankhaar
Onsala Space Observatory
Chalmers University of Technology
SE–439 92 Onsala, Sweden

Phone: +46 (0)31–772 5542
Fax: +46 (0)31–772 5590
Email: lankhaar@chalmers.se

Cover image:
The cosmic gaseous life cycle. Copyright: Marijn Lankhaar

Printed by Chalmers Reproservice
Chalmers University of Technology
Gothenburg, Sweden 2021

Tracing cosmic magnetic fields using molecules

BOY LANKHAAR
Department of Space, Earth and Environment
Chalmers University of Technology

Abstract

Understanding the magnetic field strength and morphology of astrophysical regions is of great importance to understand their dynamics. There exist a number of methods astronomers can employ to trace magnetic field structures, and each have their own limitations. This thesis focuses on tracing magnetic field using molecules.

A promising technique to trace the magnetic field morphology around evolved stars, or on the smallest scales of star forming regions, is (sub-)millimeter spectral line polarization observations. Line (linear) polarization can either arise in association with maser radiative transfer, or alternatively, molecular lines polarize through the Goldreich-Kylafis effect. In both cases, the polarization angle traces the magnetic field with a 90-degree ambiguity. In order to remove this ambiguity, and to estimate the observational viability of particular line polarization measurements, polarized line radiative transfer needs to be employed. This thesis contributes to this field in that it presents a three-dimensional polarized line radiative transfer tool: PORTAL. PORTAL simulates the emergence of thermal molecular line polarization in astrophysical objects of arbitrary geometry and magnetic field morphology. Also, this thesis introduces a novel polarization mechanism: collisional polarization. Which provides the possibility of directly detecting ambipolar diffusion in disks through the polarization of molecular ions.

Some molecules occur as masers. Masers occur naturally in specific astrophysical regions, which are often associated with highly dynamical events. Their emission is characterized by narrow lines and high brightness temperatures, and is often associated with polarization. The polarization of masers contains information on the magnetic field strength and direction of the regions they occur in. Many maser polarization observations have been performed over the last 30 years. However, one requires versatile maser polarization models that can aide in the interpretation of these observations. This thesis contributes to the study of maser polarization by presenting a modeling program called CHAMP (CHAracterizing Maser Polarization) that simulates the polarization of masers of arbitrarily high maser saturation and high angular momentum.

Methanol masers occur exclusively in association with high-mass star forming regions. They trace specific regions there, and may teach us about the magnetic field structures in the densest regions. There have been many polarization observations of methanol, but proper interpretation of them has not been possible because the molecular properties associated with its magnetic field interactions have been unknown. This thesis presents the first quantum chemical models of methanols magnetic field interactions. With them, we re-interpret the many previous methanol maser polarization observations and conclude that magnetic fields are dynamically important to the process of high-mass star formation.

Keywords: magnetic field – stars: formation – stars: evolved – stars: massive – masers – polarization

Research contributions

This thesis is based on the work contained in the following papers:

- B. Lankhaar, W.H.T. Vlemmings, G. Surcis, H.J. van Langevelde, G.C. Groenenboom, A. van der Avoird:
  Characterization of methanol as a magnetic field tracer in star-forming regions.
  Nature Astronomy, 2, 145-150 (2018).

- B. Lankhaar, W.H.T. Vlemmings:
  Characterizing maser polarization: effects of saturation, anisotropic pumping and hypefine structure.
  Astronomy & Astrophysics, 628, A14 (2019).

- B. Lankhaar, W.H.T. Vlemmings:
  PORTAL: Three-dimensional polarized (sub) millimeter line radiative transfer.
  Astronomy & Astrophysics, 636, A14 (2020).

- B. Lankhaar, W.H.T. Vlemmings:
  Collisional polarization of molecular ions: a signpost of ambipolar diffusion.
  Astronomy & Astrophysics, 638, L7 (2020).

- B. Lankhaar, W.H.T. Vlemmings, P. Bjerkeli:
  Spectral line polarization in protoplanetary disks
  Manuscript intended for submission to Astronomy & Astrophysics.

Other publications not included in this thesis

- B. Lankhaar, G.C. Groenenboom, A. van der Avoird:
  Hyperfine interactions and internal rotation in methanol.
  Journal of Chemical Physics, 145, 244301 (2016).

- D. Dall'Olio, W. H. T. Vlemmings, G. Surcis, H. Beuther, B. Lankhaar, M. V. Persson, A. M. S. Richards, and E. Varenius:
  Methanol masers reveal the magnetic field of the high mass protostar IRAS 18089-1732
  Astronomy & Astrophysics, 607, A111 (2017).

- W. H. T. Vlemmings, T. Khouri, E. O'Gorman, E. De Beck, E. Humphreys, B. Lankhaar, M. Maercker, H. Olofsson, S. Ramstedt, D. Tafoya, A. Takigawa:
  The shock-heated atmophsere of an asymptotic giant branch star resolved by ALMA.
  Nature Astronomy, 1, 848-853 (2017).

- R. Larsson, B. Lankhaar, P. Eriksson:
  Updated Zeeman effect splitting coefficients for molecular oxygen in planetary applications.
  Journal of Quantitative and Radiative Transfer, 224, 431-438 (2019).

- T. Khouri, L. Veililla-Prieto, E. De Beck, W. H. T. Vlemmings, H. Olofsson, B. Lankhaar, J.H. Black, A. Baudry:
  Detection of highly excited OH towards AGB stars - A new probe of shocked gas in the extended atmospheres.
  Astronomy & Astrophysics, 623, L1 (2019).

- W. H. T. Vlemmings, B. Lankhaar, P. Cazzoletti, C. Ceccobello, D. Dall'Olio, E. F. van Dishoeck, S. Facchini, E. M. L. Humphreys, M. V. Persson, L. Testi, J. P. Williams
  Stringent limits on the magnetic field strength in the disc of TW Hya. ALMA observations of CN polarisation.
  Astronomy & Astrophysics, 624, L7 (2019).

- R. Larsson, B. Lankhaar:
  Zeeman effect splitting coefficients for ClO, OH and NO in some Earth atmosphere applications.
  Journal of Quantitative and Radiative Transfer, 250, 107050 (2020).

- D. Dall'Olio, W. H. T. Vlemmings, B. Lankhaar and G. Surcis:
  Polarization properties of methanol masers.
  Astronomy & Astrophysics, 644, A122 (2020).

Contents

Chapter 1

Introduction

1.1 Astrophysical magnetic fields

Magnetic fields are ubiquitous in the universe. They are important to many astrophysical processes. In this thesis, we are interested in processes associated with magnetic fields in cosmic media. Particularly, we describe methods to trace magnetic fields using molecular line emission. In this section, we review the stages of the stellar evolution process, with particular emphasis on star formation and the post-main sequence phase.

Human intuition about magnetism is based on the magnetic fields that are associated with currents. Once the source of magnetism is removed, the magnetic field quickly diffuses away. Magnetic fields are only found in association with their source, which requires a constant operation in order for the magnetic field to be sustained. Indeed, on earth we are surrounded by air, which is an effective insulator. Magnetic fields that are not sustained are rapidly diffused through the process of Ohmic diffusion.

Once we leave the Earth's atmosphere we eventually find ourselves in the interstellar medium (ISM), where the gas is dilute and electrons roam almost freely. In such diffuse gases, particle collisions happen so infrequently that they can be considered effective—almost perfect—conductors (Alfvén 1963). Here, electric fields are restored almost instantaneously, and magnetic fields—once generated—are 'frozen' into the gas. Because of these properties—even though it is only partially ionized—the interstellar medium can be considered a plasma (Parker 2019).

We linger on the statement that the magnetic field is frozen into the gas of a perfect conductor. We can show this to be the case if we note the induction

equation (Shu 1991a)

$$\frac{\partial \boldsymbol{B}}{\partial t} = \eta \nabla^2 \boldsymbol{B} + \nabla \times (\boldsymbol{v} \times \boldsymbol{B}) \tag{1.1}$$

where $\boldsymbol{B}$ is the magnetic field, η is the magnetic diffusivity of the medium, and $\boldsymbol{v}$ is the bulk motion. The relative importance of both terms in the induction equation can be estimated as $\eta \nabla^2 \boldsymbol{B} \sim \eta B/L^2$ and $\nabla \times (\boldsymbol{v} \times \boldsymbol{B}) \sim VB/L$, where L is the characteristic length scale and V the characteristic velocity. The ratio between them is the magnetic Reynolds number: $R_m = LV/\eta$ and captures the relative importance of magnetic diffusion. In most astrophysical plasmas, because of their large scales and low densities, $R_m \gg 1$, and it is appropriate to ignore the diffusion term in the induction equation (Shu 1991a; Choudhuri 1998). It can be shown that the convective derivative of the magnetic flux vanishes, $\frac{d\Phi_B}{dt} = 0$, if there is no magnetic diffusion (infinite electric conductivity). This constitutes Alfvéns theorem, which states that the magnetic field passing through a surface moving with the fluid is conserved (Alfvén 1942)

$$\int_S d\boldsymbol{S} \cdot \boldsymbol{B} = \text{constant}. \tag{1.2}$$

An important implication of Alfvén's theorem is that converging gas flows have an associated increase in their magnetic field, which is why it is sometimes referred to as the flux-freezing theorem. The flux-freezing theorem is central to the progression and dynamics of astrophysical processes. To a good approximation, the flux-freezing theorem holds for almost all processes in the ISM (Kulsrud 2020). Still, non-ideal magneto-hydrodynamical (MHD) effects are important to the progression of star formation through, for instance, ambipolar diffusion (Mouschovias & Ciolek 1999). Or, on cloud scales, super-Alfvénic turbulence tends to twist magnetic field lines, thus gradually lowering the characteristic length scale, L, up to a point where non-ideal magnetic reconnection events may occur (Parker 1957; Lazarian & Vishniac 1999).

In this thesis, we focus on cosmic media; particularly, on the star-formation process in the ISM, and the shedding of evolved stellar atmospheres leading to a circumstellar medium (CSM). In the star formation process, a diffuse gas cloud collapses under its own weight to form stars which accrete the collapsing gas (Shu 1977). The gas cloud from the outset is endowed with a magnetic field that permeates the entire galaxy (Beck 2016; Crutcher 2012). The geometry of the collapse process and its relation to the magnetic field, combined with the flux-freezing theorem predicts a relation between the gas (number) density and the magnetic-field strength, often captured in the so-called power law: $B \propto n^{\kappa}$; where the constant κ is different for models with dynamically important magnetic fields (Crutcher 2012).

But, for there to be flux-freezing in astrophysical processes, we need to establish that there exists a magnetic field in the first place, because later on,

when studying the star-formation process in the next section, we take this as a given. Radio synchrotron observations of other spiral-galaxies generally reveal magnetic-field strengths of the order of $\sim$ 10 μG (Beck 2016). The magnetic fields are stronger in central starburst regions and weaker in between the spiral arms, consistent with the correlation between density and magnetic-field strength. The sustenance of the galactic magnetic field is thought to be achieved through galactic-scale dynamo action (Widrow 2002). The galactic magnetic field threads the ISM that makes up part of the galaxy and where star formation takes place. In the next section, we study the formation of stars. We will lay particular emphasis on the role of magnetic fields in the star-formation process.

1.1.1 Star formation

Part of this thesis will be focussing on the role of magnetic fields in star formation. The formation of stars is thought to occur in giant molecular clouds. Giant molecular clouds are divided up in regions of higher density that are self-gravitating clumps. These clumps contain a number of cores of still greater density, which are also self-gravitating. Each core is likely to eventually form a star or a multiple system (Draine 2010). In order for a star to form, the core must collapse under its own gravity. If we balance the stabilizing thermal gas pressure with the cores' self-gravity, we can derive the core-mass above which the cloud will collapse under its own mass: the Jeans mass (Jeans 1902). The Jeans mass is a function of the density and the gas temperature. A lot of cores are observed to be more massive than the Jeans mass, while still not dynamically collapsing. Such cores require additional stabilizing forces, often hypothesized to be found in turbulence or magnetic fields (Tan et al. 2014).

The turbulent pressure can be estimated from line-profile measurements of molecular lines in the dense cores (Elmegreen & Scalo 2004). Turbulence is seen to be present and dynamically important for the more massive cores[1], while lower mass cores are relatively unaffected by it (Tan et al. 2014). Magnetic fields permeate the entire galaxy, and thus also the dense cores. The question is if the magnetic field is strong enough to be of importance to the gas dynamics. The relative importance of the magnetic field to the gravitational collapse of the cloud is often estimated through a mass-to-flux ratio. A high mass-to-flux ratio means that gravity is stronger than the stabilizing magnetic field: the cloud is

[1]In this section, we discuss the formation of massive stars within the *Core Accretion* model. The core accretion model of massive star formation can be roughly thought of as a scaled-up version of low-mass star formation, where turbulent gas motion provides for an additional stabilization. There exist other hypotheses of massive star formation processes, of which the most important is *Competitive Accretion*. In the picture of competitive accretion, massive pre-stellar cores move through a self gravitating clump and accretes mass within a certain accretion radius, that is determined by the core mass. Massive star formation through competitive accretion leads naturally to the stellar IMF, but begins to have problems when stellar feedback and magnetic fields are being included.

magnetically supercritical, while a low mass-to-flux ratio means that the cloud is supported by a stabilizing magnetic field: the cloud is magnetically subcritical.

In a magnetically regulated process of star formation, clouds are supported by a magnetic field that threads them. Initially, the cloud is magnetically subcritical. The magnetic field does only work on the charged part of the medium, which transfers the support to the neutral medium via collisions. Since collisions happen rather infrequently, the neutral medium does not fully capture the support of the magnetic field and slips, quasi-statically, with an approximate constant velocity, inwards through gravitational contraction. This process is called ambipolar diffusion. The magnetic field is frozen to the charged medium, while the contracting neutral medium holds all the mass. So, through this contraction, the mass-to-flux ratio slowly increases to being supercritical and a dynamic collapse ensues (Mouschovias & Ciolek 1999). For solar mass stars, the magnetically regulated core collapse leads to an initial-core-mass function distribution that is in very good agreement with the initial-core-mass function derived from observations (Kunz & Mouschovias 2009). However, more massive cores are only viable through additional stabilizing turbulence (Tan et al. 2014). Still, magnetic regulation of the collapse process of massive cores can happen through ambipolar diffusion.

Numerical simulations of magnetically regulated collapse, predict that in the dynamical collapse stage, from about 10^5 cm^{-3}, the magnetic-field strength holds a relation to the number density of $B \propto n_{\rm H_2}^{0.47}$ (Mouschovias & Ciolek 1999). In the dynamical collapse phase, the mass-to-flux ratio is $2-3$ times the critical mass-to-flux ratio. In magnetically regulated star formation, the contraction of matter is along the magnetic field lines, and infall will be associated with a disk-like structure that is oriented perpendicular to the magnetic field. Additionally, the magnetic field is pinched in the perpendicular direction because of the (albeit approximate) flux-freezing of the magnetic field, and yields an hour-glass shape. Models where the magnetic field does not have a regulatory role and the collapse is randomly oriented with respect to the magnetic field, predict that the magnetic field scales $B \propto n_{\rm H_2}^{0.66}$ (Crutcher 2012).

Direct observations of the magnetic field in star-forming regions suggest that the magnetic field scales with the density as $B \propto n_{\rm H_2}^{0.65}$, while most molecular clouds are generally slightly supercritical (Crutcher et al. 2010). This results implies that magnetic fields do not fully regulate the progression of star formation, and that magnetic fields are only part of the story of the onset of star formation. Turbulence plays an additional, and possibly dominant, role. Still, turbulence is observed to be sub- or trans-Alfvénic, suggesting that magnetic fields are important to the dynamics of turbulence. Additionally, on the smaller scales of star formation magnetic fields are important to a range of processes, whose feedback to the cloud-scale affects the generation and maintenance of turbulent processes (Krumholz & Federrath 2019).

We move on to the smaller scales of star formation, and follow the material

that collapses towards the centre of a core. The collapsing core is from the outset endowed with a small net rotation (Krumholz 2015). When the mass of the core is infalling, nature requires that angular momentum be conserved. Therefore, matter that is infalling will increase its rotational energy, and through this, form a disk like structure. In the centre of the disk (and the collapsing region), a protostar has had time to form. In order for mass to accrete onto the protostar, angular momentum has to be transported outwards. This can occur through viscous tension, provided the viscosity of the disk gas is amplified by turbulence (Pringle 1981). The turbulence in turn can form through instabilities such as the magneto-rotational instability (Balbus & Hawley 1991). Other means of angular momentum transport are magnetic tensions between the toroidal and radial part of the magnetic field, or the formation of an outflow structure. Outflows that are bipolar in structure are often seen in association with accretion disks, and they are thought to be launched by magnetic fields (Blandford & Payne 1982; Shu et al. 2000; Bjerkeli et al. 2016).

The accretion onto the protostar lessens with time and demands on the fast removal of angular momentum are diminished. The outflow dies out and—for the lower mass stars—a quasi-stationary disk forms in which the dust has time to coagulate and increase in size, while the gravitational contraction of the protostar has raised the temperature there enough to drive hydrogen nuclear fusion, which takes over as the main-energy source of the protostar. The star has thus entered its 'main-sequence'. The persistent luminosity of the star blows away most of the disk material that has accrued over the star-formation process, while possible planet- and comet-sized objects remain to revolve around it.

1.1.2 The outflows of evolved stars

The magnetic field that made up the collapsing core from the beginning is partially transferred to the central star through its coupling to the gas. It should be said though that processes such as ambipolar diffusion and Ohmic dissipation have weakened the magnetic field further. Still, all stars on the main-sequence are thought to be associated with a magnetic field (Berdyugina 2008). Some of the magnetized stars are characterized by a magnetic field that is relatively stable over time. These are believed to host a magnetic field that is the remnant of the ISM magnetic field, amplified by the contraction (Braithwaite & Spruit 2004). While other stars, such as our Sun, have a magnetic field that is highly variable over time. Such magnetic fields have to be sustained by a stellar dynamo, likely driven by stellar rotation in combination with convection (Parker 1955).

When solar-type main-sequence star runs out of hydrogen in its core, it expands and cools down in its evolution along the red giant branch (RGB). While the outer layers of an RGB star cool down, gravitational contraction heats up its core further up to the point when it becomes hot enough to fuse helium. After

exhausting the central helium, the stellar envelope expands for a second time, and the star goes over to evolve along the asymptotic giant branch (AGB) (Habing & Olofsson 2013). The expansion of the star weakens the magnetic-field strength because of flux-freezing. Additionally, the stellar evolution processes likely have an impact on the stellar dynamo-action, and the magnetic field changes accordingly. Few direct observations exist of AGB stellar surface magnetic fields (Vlemmings 2018). The usual method of Zeeman-Doppler imaging is not sensitive enough for the (in comparison to main-sequence stars) weaker magnetic fields of AGB stars (see Eq. (3.35)).

The atmosphere of the AGB star is slowly shedding a stellar wind, thus forming a circumstellar medium. In the extended atmosphere of AGB-type stars, the relatively low temperature allows for certain molecules to adhere in complexes that are generally referred to as dust (Gail & Sedlmayr 2014). Momentum carried by the light that luminates from the central star is transferred to the dust through its broad-band absorption or scattering. This drives a strong stellar wind that results in significant mass loss of the AGB star (Lamers et al. 1999). A magnetic field could have a significant impact on the wind-formation in AGB stellar atmospheres. For instance, Alfvén waves could add to the acceleration of the wind (Falceta-Gonçalves & Jatenco-Pereira 2002), or they can create cool spots on the stellar surface so that dust could form more easily there (Soker 1998; Vlemmings 2018). As to the internal stellar structure, magnetic fields affect nuclear fusion processes, through MHD-induced internal mixing, that can significantly impact the stellar yields (Trippella et al. 2016).

The loss of stellar mass in the AGB phase is an important feature of the galactic gaseous life-cycle as it enriches the ISM with the elements produced through the stars' life, as well as providing seeds for dust production in the ISM (Habing & Olofsson 2013). The high mass-loss of the AGB star limits its lifetime to about 10^6 yr. After losing essentially all of its envelope, the star starts heating up, while maintaining approximately the same luminosity. It has now entered the post-AGB phase. The stellar wind in the post-AGB phase is characterized by a lower mass loss, but is associated with large outflow velocities, which are sometimes bipolar in their geometry (Van Winckel 2003). The stellar wind from the AGB phase has built an envelope of gas and into which the post-AGB wind crashes. If the conditions are suitable, the envelope gas is ionized and emits as a Planetary Nebula (Kwok et al. 1978). Planetary Nebulae manifest elaborate geometries that require equally elaborate wind expulsion mechanisms to be explained (Balick & Frank 2002). Magnetic fields might play an important role here, too (Nordhaus et al. 2007; Balick & Frank 2002).

1.2 Observations of cosmic magnetic fields

Cosmic magnetic fields have been observed in a variety of ways. We review the range of methods that astronomers employ to measure both the strength and morphology of magnetic field structures in astrophysical objects.

On the galactic scale, radio astronomers have identified that a significant part of the emission in the radio part of the spectrum is due to synchrotron emission. Synchrotron radiation is produced by highly energetic electrons traveling in a path that is curved with respect to the magnetic field (Shu 1991b). Synchrotron radiation has a characteristic intensity-frequency relation and can be identified through a broad spectral analysis; its emission is also partially polarized (Rybicki & Lightman 2008) and may reveal the properties of the magnetic field that gave rise to the emission.

On smaller scales, of the order of molecular clouds, we require different mechanisms to trace magnetic fields, since the high-energetic electrons are not present. Galactic molecular clouds span rather large angular scales, and for a global analysis, single-dish observations will have the appropriate angular resolution. Molecular clouds can be traced through the observation of molecular lines, typically in the radio to the submillimeter region of the spectrum. Alternatively, the interstellar dust that makes up about a percent of the molecular cloud mass may be observed, typically in the infrared part of the spectrum.

Some molecular emission lines may be used as tracers of the magnetic-field strength. Those molecules that have unpaired electrons—paramagnetic molecules—exhibit particularly strong Zeeman effects (section 3.2.2). Zeeman effects can be seen in the circular polarization of spectral lines, and are sensitive to the line-of-sight magnetic field (Crutcher & Kemball 2019). Molecular lines can also be used as tracers of the magnetic field morphology. Through the so-called Goldreich-Kylafis (GK) effect (section 4.3), rotational lines tend to be linearly polarized in the direction parallel or perpendicular to the magnetic field, provided that an anisotropic velocity gradient as well as relatively low densities characterize the emission region (Goldreich & Kylafis 1981).

Most notable polarized dust continuum observations of molecular clouds come from the Planck space telescope, that mapped dust emission in the far-infrared (FIR) region of the spectrum (Ade et al. 2015), the air-borne observatory SOFIA, that can go up to mid-IR frequencies (e.g. Chuss et al. 2019) and ALMA (Hull & Zhang 2019). Tracing cloud structures through polarized observations, they show the dust emission to be significantly polarized. This is believed to occur through the Radiative Torque Alignment (RAT) mechanism, where an anisotropic radiation field 'spins up' (non-spherical) dust particles to precess around the magnetic field axis (Lazarian & Hoang 2007). Thus, on average, the dust particles are

aligned with the magnetic field and their polarized emission traces the magnetic field structure. The magnetic-field strength can be estimated by comparing the scatter in the dust polarization angles to the turbulence—where the turbulence is gauged by co-spatial line-profile measurements. The comparison gives an indication of the ratio of turbulent and magnetic energy; and thus is a gauge for the magnetic field strength (Davis Jr & Greenstein 1951; Chandrasekhar & Fermi 1953; Houde et al. 2009). This method is referred to as the Chandrasekhar-Fermi method, and gives an order-of-magnitude estimate of the magnetic-field strength.

We need yet better angular resolution to trace smaller scales of star formation; closer to the protostar. (Sub-)millimeter observations using the Atacama Large Millimeter/submillimter Array (ALMA) interferometer may be employed for this. Tracing magnetic fields in the (sub)millimeter regime close ($\lesssim 100$ AU) to the protostar has proven more difficult using dust polarization observations. In these warmer regions, where a clear disk geometry has manifested in the gas (and dust) structure, and an intricate radiation morphology is present, alternative alignment mechanisms may determine the spinning properties of the dust (Kataoka et al. 2015, 2017; Stephens et al. 2017). This gives rise to polarized emission that does not trace the magnetic field structure. Such polarized dust emission maps may be used to trace other properties of these small-scale star-forming regions, but for magnetic field morphology measurements, we have to defer to spectral line polarization measurements. It can be shown that GK polarization does trace the magnetic field, also in these regions (see Chapter 3). However, the polarization mechanism of molecular spectral lines in the complicated star-forming geometries cannot be viably modeled through the large velocity gradient (LVG) approximation that characterizes the standard GK effect (see section 4.3). Rather, three-dimensional modeling of the polarized radiation transport is required. This is what we present in paper III of this thesis.

When the star-formation process is done and the star enters its main-sequence, its magnetic field can be gauged through Zeeman-Doppler imaging of atomic line transitions in the optical (Semel 1989). In particular, such measurements of the Sun have yielded magnetic field maps of high resolution, that show a very complicated—but approximately dipolar—magnetic field structure of the Sun's surface. Also, magnetic fields are closely related to many processes on the Sun's surface that are associated with its mass-loss (Choudhuri 1998). Typical solar surface magnetic-field strengths are on the order of $\sim$ G, while the magnetic fields of sunspots can go up to $\sim$ kG field strengths (Zwaan 1987).

After their main sequence evolution, solar-type stars eventually enter the AGB phase, which is partially characterized by a strong mass loss through a stellar wind. Optical observations of the stellar surface are often obscured, and the magnetic field has weakened because of the stellar expansion, so Zeeman-Doppler imaging is of limited utility. Close to the stellar surface, SiO masers are excited in rotational lines at millimiter and submillimeter wavelengths, and show partic-

ularly high degrees of polarization, both circular and linear (Cotton et al. 2004). The polarization might trace the magnetic field morphology and strength, but a better understanding of the excitation mechanism, and how it pertains to SiO masers' polarization properties is required to draw definitive conclusions (see also Paper II). Outflows that are seen in some AGB and post-AGB objects, are associated with maser-lines from H_2O and OH (Gray 2012). These maser-lines can be studied for magnetic field signatures in their polarization properties (Vlemmings & van Langevelde 2005; Vlemmings et al. 2006; Rudnitski et al. 2010). Thermal lines are significantly affected by the central stellar emission and may be polarized (Morris et al. 1985). This also requires proper three-dimensional radiative transfer modeling to be interpreted (Paper III and Vlemmings et al. in prep.).

1.3 Motivation of this thesis

In this introduction, we have stressed the importance of magnetic fields to all the stages of stellar evolution, and the difficulties of measuring them, particularly on the smallest scales of star-formation processes and in the vicinity of evolved stellar objects, that lose much of their mass in a stellar wind. We contend that tracing magnetic fields in these regions through the polarization of molecular lines is a viable and promising method. We briefly outline the contributions that this thesis makes in this endeavor.

To trace the densest regions of the ISM, close to stellar objects, interferometers with high angular resolution are required. Of these, the most recent and advanced is the ALMA telescope. ALMA has recently commissioned full polarization capabilities, allowing for the observation of these star-forming regions at the smallest scales while utilizing the polarization capabilities to give information on the magnetic field.

Alternatively, masers have been traditionally used as probes in the denser parts of (high-mass) star-forming regions, where they are often associated with accretion flows and feedback processes. Masers have also been used as tracers of the gas close to the AGB stellar surface of AGB stars, in regions before the dust condensates, and in the (bipolar) outflows of some AGB/post-AGB objects. Masers radiate optimally in the radio to millimeter/submillimeter part of the spectrum, and they are particularly suited to high-resolution imaging through Very Long Baseline Interferometry (VLBI).

As significant strides have been made in developing polarized interferometry capabilities to observe astrophysical processes on the smallest scales, the development of radiative transfer modeling tools to interpret the polarized signals from these regions has been lacking. In this thesis we present such tools, both for thermal line emission in (sub)millimeter spectral lines (Paper III, V), as well as for

one-dimensional maser propagation through a medium permeated by a magnetic field (Paper II).

We dedicate particular attention to the molecular physics of the Zeeman effect of a particular maser species that traces dense regions of high-mass star-forming regions: methanol (CH_3OH). Over the years, many maser polarization observations of this species have been performed (e.g. Vlemmings et al. 2011), but a rigorous model for its complicated Zeeman effect has never been presented. Paper I presents a first-principles model of methanols Zeeman effect, that also takes into account the effects of torsional motion of the OH-group with respect to the CH_3 group.

We have at many points in this introduction stressed the importance of ambipolar diffusion in the star-formation process. Still, telescope observations have not been able to show the presence of this process through direct observation (Yen et al. 2018). In Paper IV, we present a hypothesis, that the presence of an ambipolar diffusion induced drift-velocity gives rise to a partial alignment of molecular ions, because their collisions with the main collision partner H_2 have a preferential direction. We show that on the smallest scales of star formation, within ~ 100 AU of the accreting protostar, this process will give rise to detectable polarization in the emission, that traces the magnetic field direction, as well as provide direct evidence for the process of ambipolar diffusion.

Chapter 2

Light

The senses of the astronomer are limited. Astronomers are almost exclusively bound to inferring the properties of night-sky objects from the electromagnetic radiation they emit. Modern astronomers can also enlist high-energy particles and even gravitational waves as sources of information; but still, most of astrophysics is based on the observation of light. The earliest astronomers had to limit themselves to observation of electromagnetic radiation in the visible spectrum, but nowadays also the radio, infrared, UV and X-ray part of the electromagnetic spectrum have become available for astronomical observations as well.

In this chapter, we revisit the properties of light. To fully appreciate the work contained in this thesis, we lay particular emphasis on two properties of light: coherence and polarization. In most astronomical observations, both the coherence and polarization properties of light are ignored. Coherence might be an important factor in the transfer of radiation in masers, while the polarization properties of light are indicative of a particular alignment of the emitting region. In the following section, we introduce the radiative transfer equation and define the specific intensity of light. After that, we relate this to the polarization properties of light. We end this chapter by discussing the use of light in this thesis.

2.1 Radiative transfer equation

From the definition of how light is measured, we describe some of its properties and introduce the radiative transfer equation that characterizes the transport of radiation in astrophysical media.

When we measure light, we measure the total energy of the light ray, dE, that passes per unit area, dA, per unit time, dt, per unit frequency, $d\nu$, and per unit

solid angle, $d\Omega$ (Chandrasekhar 2013)

$$I_\nu = \frac{dE}{dAdtd\nu d\Omega}. \tag{2.1}$$

The quantity, I_ν, is called the specific intensity. It can be related to the density of states in phases space, $\mathcal{N} = dN/dV_x dV_p$, where N is the number of photons, and V_x and V_p represent the volume in physical and momentum space. By using $dE = h\nu dN$, $dV_p = (h/c)^3\nu^2 d\Omega d\nu$ and $dV_x = cdtdA$, we have the density of states (Thorne & Blandford 2017)

$$\mathcal{N} = \frac{c^2}{h^4}\frac{I_\nu}{\nu^3}. \tag{2.2}$$

Assuming that the (bosonic) photons are in statistical equilibrium, at some temperature, T, we have the standard bosonic distribution function (Landau et al. 1980)

$$\mathcal{N}_{\text{s.e.}} = \frac{2}{h^3}\frac{1}{e^{h\nu/kT} - 1}, \tag{2.3}$$

where the factor 2 comes from the photon energy degeneracy. A photon gas that is in thermal equilibrium, thus has a specific intensity

$$\begin{aligned} B_\nu(T) &= \frac{h^4\nu^3}{c^2}\mathcal{N}_{\text{s.e.}} \\ &= \frac{2h\nu^3}{c^2}\frac{1}{e^{h\nu/kT} - 1}, \end{aligned} \tag{2.4}$$

which is the Planck function.

Now, we consider a ray of light moving through some medium. The changes to the specific intensity can be described by the convective derivative (Shu 1991b)

$$\begin{aligned} \frac{1}{c}\left(\frac{\partial}{\partial t} + \boldsymbol{v}\cdot\nabla\right) I_\nu &= \text{sources} - \text{sinks}, \\ \left(\frac{\partial}{\partial ct} + \boldsymbol{n}\cdot\nabla\right) I_\nu &= \epsilon_\nu - \kappa_\nu I_\nu, \end{aligned} \tag{2.5a}$$

where c and $\hat{\boldsymbol{n}}$ are the speed and direction of the light ray, ϵ_ν is the emissivity of the medium and κ_ν is the absorption coefficient of the medium. In this thesis, we are predominantly interested in the interaction of light with molecules. We present the appropriate absorption and emissivity coefficients for a molecular medium in section 4.1. At the frequencies that we are interested in in this thesis, it is safe

to ignore scattering of radiation in the radiative transfer. One can compute the propagation of the specific intensity of a ray of light (in the Lagrangian frame) as

$$\frac{d}{ds}I_\nu = \epsilon_\nu - \kappa_\nu I_\nu,$$
$$\frac{d}{d\tau_\nu}I_\nu = S_\nu - I_\nu, \tag{2.5b}$$

where we define τ_ν as the optical depth; and $S_\nu = \epsilon_\nu/\kappa_\nu$ is the source function. For a medium in thermal equilibrium $S_\nu \to B_\nu(T)$; so that under optically thick conditions, the specific intensity will converge to $I_\nu \to B_\nu(T)$, thermal radiation.

2.2 Polarization and coherence properties of light

Up to now, we upheld a fluid-like description of electromagnetic radiation—as particles traveling through a medium of sources and sinks. To appreciate more deeply some of the properties of light that will interest us, we will take a step back and consider the light as oscillating electric and magnetic fields. While doing this, we dedicate particular attention to the polarization and coherence properties of light.

To start off, we note the Maxwell Equations (Jackson 1998)

$$\nabla \cdot \boldsymbol{E} = 4\pi\rho_e, \qquad \nabla \cdot \boldsymbol{B} = 0,$$
$$\nabla \times \boldsymbol{E} = -\frac{1}{c}\frac{\partial \boldsymbol{B}}{\partial t}, \qquad \nabla \times \boldsymbol{B} = \frac{4\pi}{c}\boldsymbol{j}_e + \frac{1}{c}\frac{\partial \boldsymbol{E}}{\partial t}, \tag{2.6}$$

that relate the electric and magnetic fields, $\boldsymbol{E}$ and $\boldsymbol{B}$ to each other, and the current density, $\boldsymbol{j}_e$ and charge density ρ_e. In a vacuum, the charge density and electric current are both zero: $\rho_e = 0$ and $\boldsymbol{j}_e = 0$. Then, under vacuum conditions, the following wave equations can be derived from the Maxwell equations

$$\left(\frac{\partial^2}{\partial t^2} - c\frac{\partial^2}{\partial z^2}\right)\boldsymbol{E} = 0, \tag{2.7a}$$
$$\left(\frac{\partial^2}{\partial t^2} - c\frac{\partial^2}{\partial z^2}\right)\boldsymbol{B} = 0, \tag{2.7b}$$

which has the general solution propagating in the $\pm z$ directions (Shu 1991b)

$$\boldsymbol{E} = \boldsymbol{E}_+(z - ct) + \boldsymbol{E}_-(z + ct), \tag{2.8a}$$
$$\boldsymbol{B} = \boldsymbol{B}_+(z - ct) + \boldsymbol{B}_-(z + ct), \tag{2.8b}$$

where $\nabla \cdot \boldsymbol{E} = \nabla \cdot \boldsymbol{B} = 0$ implies $\boldsymbol{z} \cdot \boldsymbol{E}_{\pm} = \boldsymbol{z} \cdot \boldsymbol{B}_{\pm} = 0$, and we have the electric and magnetic field components of the electromagnetic wave perpendicular to each other: $\boldsymbol{B}_{\pm} = \pm \boldsymbol{z} \times \boldsymbol{E}_{\pm}$. We posed the solution to the Maxwell equations in vacuum, Eq. (2.8), generally, but for our purposes it leads to better insight if we specify our solution to a monochromatic wave with frequency, ν, propagating in the $+z$ direction. The solution for the electric field then, is trivially (Shu 1991b)

$$\boldsymbol{E}_{\nu}(z - ct) = \mathrm{Re}\left[\left(\hat{\boldsymbol{e}}_x \tilde{\mathcal{E}}_x + \hat{\boldsymbol{e}}_y \tilde{\mathcal{E}}_y\right) e^{2\pi i \nu (z/c - t)}\right], \tag{2.9}$$

where $\tilde{\mathcal{E}}_{x,y}$ are the complex electric field amplitudes of the x and y-components of the radiation field.

It may be noted in the description of the monochromatic wave traveling in the $\hat{\boldsymbol{z}}$-direction, that four variable factors describe the properties of the traveling EM-wave (the amplitudes $\mathcal{E}_{x,y}$ and their phases $\phi_{x,y}$). This may be contrasted to our earlier fluid-like description of light, where only the specific intensity, I_{ν}, was used to describe a ray of light. Indeed, if we had only been concerned with the total energy flux of the electromagnetic wave, the total energy flux density

$$I_{\nu} = \frac{c}{8\pi}\left(\left|\tilde{\mathcal{E}}_x\right|^2 + \left|\tilde{\mathcal{E}}_y\right|^2\right), \tag{2.10a}$$

is the only parameter of interest. However, directional properties of light may also be detected, and are conveniently described as the Stokes polarization parameters

$$Q_{\nu} = \frac{c}{8\pi}\left(\left|\tilde{\mathcal{E}}_x\right|^2 - \left|\tilde{\mathcal{E}}_y\right|^2\right), \tag{2.10b}$$

$$U_{\nu} = \frac{c}{4\pi}\mathrm{Re}\left[\tilde{\mathcal{E}}_x \tilde{\mathcal{E}}_y^*\right], \tag{2.10c}$$

$$V_{\nu} = \frac{c}{4\pi}\mathrm{Im}\left[\tilde{\mathcal{E}}_x \tilde{\mathcal{E}}_y^*\right]. \tag{2.10d}$$

These additional Stokes parameters hold information about the directional properties of the radiation. In this thesis, we will endeavor to obtain information of the preferential alignment of molecules in astrophysical environments due to—mainly—magnetic fields. Aligned molecules emit preferentially oriented radiation, which is reflected in the Q-, U- and V-components of the Stokes parameters.

The Stokes parameters that we derived from a monochromatic single wave are fully polarized,

$$I_{\nu}^2 = Q_{\nu}^2 + U_{\nu}^2 + V_{\nu}^2. \tag{2.11}$$

However, in reality, and particularly in astrophysical context, the light that is observed is an ensemble of many EM-waves. These EM-waves are caught by a

detector over a period of time, and the Stokes parameters are measured as a time-average

$$I = \frac{c}{8\pi}\left(\langle\left|\tilde{\mathcal{E}}_x\right|^2\rangle + \langle\left|\tilde{\mathcal{E}}_y\right|^2\rangle\right), \tag{2.12a}$$

$$Q = \frac{c}{8\pi}\left(\langle\left|\tilde{\mathcal{E}}_x\right|^2\rangle - \langle\left|\tilde{\mathcal{E}}_y\right|^2\rangle\right), \tag{2.12b}$$

$$U = \frac{c}{4\pi}\mathrm{Re}\left[\langle\tilde{\mathcal{E}}_x\tilde{\mathcal{E}}_y^*\rangle\right], \tag{2.12c}$$

$$V = \frac{c}{4\pi}\mathrm{Im}\left[\langle\tilde{\mathcal{E}}_x\tilde{\mathcal{E}}_y^*\rangle\right], \tag{2.12d}$$

which relaxes the condition (Chandrasekhar 2013)

$$I^2 \geq Q^2 + U^2 + V^2, \tag{2.13}$$

and also allows for partially polarized light. The time average $\langle\tilde{\mathcal{E}}_p\tilde{\mathcal{E}}_{p'}^*\rangle$ includes all EM waves, with arbitrary frequencies. We can relate the time-dependent electric field to its frequency components through a Fourier decomposition

$$\tilde{\mathcal{E}}_p = \frac{1}{\sqrt{2\pi}}\int_{-\infty}^{\infty} d(2\pi\nu)\tilde{\mathcal{E}}_p(\nu)e^{-2\pi i\nu(t-z/c)}. \tag{2.14}$$

For non-coherent light, it may be shown that (Elitzur 1992)

$$\langle\tilde{\mathcal{E}}_p(\nu)\tilde{\mathcal{E}}_{p'}^*(\nu')\rangle = \langle\tilde{\mathcal{E}}_p(\nu)\tilde{\mathcal{E}}_{p'}^*(\nu)\rangle\,\delta(\nu-\nu'), \tag{2.15}$$

which allows for the formulation of the Stokes parameters per frequency; and in the same dimension as the specific intensity.

Coherence is said to be present in radiation if the phases of ensembles of EM waves of different frequency (temporal coherence) or position (spatial coherence) are linked. When light is temporally coherent, the statistically random average we take in Eq. (2.15) no longer applies, which has deep consequences for matter-radiation interactions. Since we are interested in maser radiation in this thesis, it is necessary to linger on the coherence properties of EM radiation of astrophysical masers. In particular because the laboratory counterpart of the astrophysical maser—as well as laboratory lasers—possess a high degree of coherence in their radiation.

For this discussion, it is worth pointing out one important difference between laboratory and astrophysical masers. In order for maser radiation to build up, one needs a long column of population inverted particles (the maser medium). Since laboratories are generally confined to scales of the order of meters or less, this presents a challenge. Experimentalists circumvent this problem by placing on either side of the maser medium a mirror, which reflects back and forth the maser radiation, thereby increasing the maser path length with some orders of magnitude,

but also enhancing the spatial and temporal coherence of the maser radiation due to interference effects.

This is in contrast to masers on astrophysical scales, where maser path lengths are sufficiently long to lead to significant amplification of radiation by way of stimulated emission. Because of the large path lengths ($\ell/\lambda \sim 10^{14}$), maser radiation is only spatially coherent for rays that propagate on within small angles $\Delta\Omega \ll \lambda/\ell$ (Elitzur 1992), which is well below the maser beaming angles (see chapter 4) of $\Delta\Omega = 10^{-4} - 10^{-2}$ that are inferred from observations. Temporal coherence only manifests in astrophysical masers when stimulated emission events are occurring at a higher rate, R, than statistical fluctuations in the maser radiation, represented by its line-width (in angular frequency units), $\Delta\omega$. However, such high rates of stimulated emission are not observed for astrophysical masers (Elitzur 1992; Gray 2012). It has been suggested that coherence effects in astrophysical maser radiation give rise to the pulsed nature of some of the periodic masers through global superradiant states (Dicke 1954) in a very thin slice of velocity-space (Rajabi & Houde 2020). One critical difference between theories of superradiance and maser theory is their assumed lifetimes of the states participating in the maser/superradiant transition.

Observations of the temporal coherence properties of astrophysical maser radiation are necessary to determine the coherent nature of the stimulated emission processes in population inverted regions. Considering that most maser sources are relatively long-lived, and that their decay-rates—obtained from line-profile observations and maser excitation modeling—are too high for significant temporal coherence to build up, we assume throughout this thesis that astrophysical maser emission is non-coherent.

2.3 The use of light in this thesis

We opened this thesis by highlighting the importance of magnetic fields in astrophysical processes. It is very difficult to observe magnetic fields in astrophysical regions directly. Magnetic fields do not leave a trace in the emission of radiation when one only observes the total intensity of the light emerging from these regions. Instead, the polarization of light has to be analyzed to obtain information on the directional properties of the region of interest. In this thesis, we characterize the polarization properties of light that emerges from molecular lines that are affected by magnetic fields.

In the (sub)millimeter regime, relevant to the ALMA (Atacama Large (sub)Millimetre Array) telescope, emission comes predominantly from molecules—in the form of line-emission—and dust—in the form of continuum emission. Magnetic fields indirectly work on both molecules and dust and tend to partially align part of the

populations of these species. A consequence of this is that the (sub)millimeter light emission coming from these partially aligned species also has a preferred direction for the oscillating electric field: the emission is partially polarized. The direction of polarization is indicative of the magnetic field direction; and by studying the polarization of radiation, one can infer the magnetic field morphology of the region under study.

Dust polarization has proven itself to be a very useful tool to study the magnetic field morphology of astrophysical star forming regions on molecular cloud scales. However, going to smaller scales of star formation—in the direct vicinity of forming protostars—the alignment of dust is affected through other mechanisms, and dust-polarization therefore does not trace magnetic field morphologies faithfully. Also, in atmospheres of evolved stars, dust formation is ongoing, but dust emission is too diffuse to be viably used for polarization analysis.

To study magnetic fields in these regions, we thus have to resort to the observation of molecular line polarization. However, while significant strides have been made in developing polarized interferometry capabilities to observe astrophysical processes on the smallest angular scales, theories of molecular line polarization are based on approximations that are not applicable to, for instance, the small-scale regions of star-formation or evolved stellar envelopes. Part of this thesis focuses on developing new theoretical tools that are to be used in conjunction with polarized interferometry of molecular line emission, to obtain accurate information on the magnetic field morphology of the astrophysical regions they are excited in.

A special case of line emission, 'masing', is found in some regions (see section 4.2). Masers (Microwave Amplified by Stimulated Emission of Radiation), because of their highly 'beamed' geometry, are in good approximation described by one-dimensional propagation. The almost one-dimensional propagation in conjunction with a magnetic field results in partial alignment of the maser medium, which emits polarized emission that traces the magnetic field direction. Furthermore, masers, because of their extreme brightness temperatures and narrow line profiles, can also be used to infer magnetic field strength through direct observations of the splitting of the emission lines through the Zeeman effect. In this thesis, we develop a theoretical quantum-chemical model to quantify Zeeman splitting effects for methanol (Paper I): a non-rigid rotor system with a complicated hyperfine structure, and we present a radiative transfer program, that characterizes the maser polarization profile for masers at arbitrary magnetic field strength, direction and maser brightness temperature; and investigates alternative ways to produce maser polarization (Paper II).

Chapter 3

Molecules

Much of the material that exists between the stars, the interstellar medium (ISM), is found in molecular form. In this chapter, we review the molecular physics that is relevant to radio astronomy. Because it is the main theme of this thesis, we dedicate extra attention to effects that can lead to the alignment of molecular species, and thus to the polarization in the radiation that emerges from ISM regions.

In the following section, we review the basic molecular physics of isolated molecules. Thereafter, we describe the interaction of isolated molecules with magnetic—both internal and external—and electric fields. In the final section, we linger on the the directional nature of molecular interactions with external electric and magnetic fields; this will serve as a preamble to the next chapter.

3.1 Basic molecular physics

Molecules in the ISM spend the vast majority of their time as isolated particles. To describe the dynamics of individual molecules, we consider the motions of the electrons and nuclei that make up a molecule. We identify three types of molecular motion: electronic, vibrational and rotational motions. To a reasonable approximation, these types of motion can be studied in isolation. In this section, we review the (quantum-mechanical) description of internal dynamics of molecules.

Densities in the ISM are exceedingly low. In the cold neutral medium, the number of H_2 molecules found in a cubic centimeter, the number density, is on the order of 10^4 cm^{-3}. But in sites of ongoing dynamical events, such as accretion, number densities can rise to higher values. Typical mean-free paths of molecules in the ISM are

$$l_{\mathrm{mfp}} = 10^{10} \left(\frac{\sigma}{1\ \text{Å}^2} \right)^{-1} \left(\frac{n_{\mathrm{H_2}}}{10^6\ \mathrm{cm}^{-3}} \right)^{-1}\ \mathrm{cm},$$

where σ is the collisional cross-section. For a species in the ISM with a typical thermal velocity of $\sim$ 1 km/s, this would mean that it would take about a day before that species interacts with another constituent of the ISM. When we furthermore consider that this interaction takes about a picosecond, it is clear that we can consider the molecular constituents of the ISM as individual particles, with their associated properties unperturbed by the interaction with other particles of the ISM.

The physics of isolated molecules is most effectively described by considering the motion of the electrons and nuclei that they consist of. We will start our discussion by considering the motion of the electrons that make up a molecule. We consider a poly-atomic molecule with N_n nuclei and N_e electrons. The coordinates of nucleus, α, are $\boldsymbol{r}_\alpha$ and have an associated mass m_α and charge $Z_\alpha e$, where e is the elementary charge. We let the coordinates of electron, i, be $\boldsymbol{r}_i$, and all electrons have mass m_e and charge $-e$. The Hamiltonian of this system is the sum of the electron- and nuclear-motion energies and the attractive and repulsive Coulomb-energies (Szabo & Ostlund 2012)

$$\hat{H} = -\sum_i \frac{\hbar^2}{2m_e}\nabla_i^2 - \sum_\alpha \frac{\hbar^2}{2m_\alpha}\nabla_\alpha^2 - \sum_{i\alpha} \frac{Z_\alpha e^2}{4\pi\epsilon_0 r_{i\alpha}} + \sum_{ij} \frac{e^2}{4\pi\epsilon_0 r_{ij}} + \sum_{\alpha\beta} \frac{Z_\alpha Z_\beta e^2}{4\pi\epsilon_0 r_{\alpha\beta}}, \quad (3.1)$$

where ϵ_0 is the vacuum permittivity and r_{ij} is a short-hand notation for the distance between the vectors $|\boldsymbol{r}_i - \boldsymbol{r}_j|$. The motion of the nuclei and electrons are not strictly separated according to this general molecular Hamiltonian. But considering that the motion of the nuclei is much slower than that of the electrons, the nuclear and electronic motion can be separated through the Born-Oppenheimer approximation (Born & Oppenheimer 1927).

In our discussion of the structure of molecules, we assume the electronic structure to be 'closed-shell': that is, there are no unpaired electrons. It is certainly possible to perform calculations to the electronic structure of 'open-shell' molecules, but we will refrain from such a discussion in this thesis. This will also simplify our coming discussion on the nuclear motions of molecules, because spectral fine-structure that is introduced by interactions with the unpaired electrons can be neglected (Brown & Carrington 2003). For the purposes of this thesis, where we consider the alignment of molecules, and considering that most astrophysical molecules are closed-shell, these approximations will do. However, open-shell molecules are extremely important in tracing magnetic field strengths in astrophysical regions, as the unpaired electrons give rise to a paramagnetic Zeeman effect that is 3 orders of magnitude greater than the Zeeman effects we will be considering in this thesis (Crutcher & Kemball 2019). The resulting spectral decoupling of the circularly polarized transitions can be directly observed already for weak magnetic fields, and has provided astronomers with solid information on magnetic field strengths in astrophysical regions (Crutcher 2012).

3.1.1 Electronic motion

We assume that the nuclei are stationary on the timescale of electronic motion and thus separate the molecular Hamiltonian in a kinetic nuclear part, and an electronic part,

$$\hat{H}_{\text{el}} = -\sum_i \frac{\hbar^2}{2m_e}\nabla_i^2 - \sum_{i\alpha} \frac{Z_\alpha e^2}{4\pi\epsilon_0 r_{i\alpha}} + \sum_{ij} \frac{e^2}{4\pi\epsilon_0 r_{ij}} + \sum_{\alpha\beta} \frac{Z_\alpha Z_\beta e^2}{4\pi\epsilon_0 r_{\alpha\beta}}, \tag{3.2}$$

$$\hat{H}_{\text{nuc}} = -\sum_\alpha \frac{\hbar^2}{2m_\alpha}\nabla_\alpha^2. \tag{3.3}$$

We will consider the nuclear Hamiltonian at a later stage. Now, we will briefly consider the electronic part of the molecular Hamiltonian.

It is beyond the scope of this thesis to work out the full methodology behind solving the molecular electronic Hamiltonian. It will however be helpful if we consider briefly and qualitatively the steps modern quantum chemists take to find the solution to $\hat{H}_{\text{el}}$. First, it has to be conceded that finding the 'exact' solution to the time-independent Schrödinger equation,

$$\hat{H}_{\text{el}}\psi_{\text{el}}(\{\boldsymbol{r}_i\};\{\boldsymbol{r}_\alpha\}) = E_{\text{el}}\psi_{\text{el}}(\{\boldsymbol{r}_i\};\{\boldsymbol{r}_\alpha\}), \tag{3.4}$$

is not possible considering the two-particle interaction term contained in the electron-electron Coulomb repulsion (Szabo & Ostlund 2012). To solve the eigenvalue problem, we have to work around the two-particle operator while keeping the problem tractable. First, we define a basis of wave functions within which the solution of the eigenvalue problem is going to be sought. These basis functions are based on the hydrogen-atom-like orbitals that are the solutions of the electronic Hamiltonian of an hydrogen-like-atom (Helgaker et al. 2014). The orbital functions are tweaked in order to be conveniently integrated and they are specific to each nucleus. The basis can be infinitely big but is truncated to make solving Eq. (3.4) feasible. The total eigenfunctions ψ_{el} are described as Slater determinants of the basis functions to make sure that the fermionic requirement of anti-symmetry is fulfilled.

But even inside the truncated basis it is not possible to directly solve Eq. (3.4) due to the two-particle operator of the electron-electron Coulomb repulsion term. To reduce this term to a one-electron operator, one employs the mean-field approximation: the electron-electron interaction between the individual electrons is approximated by those electrons interacting instead with a 'mean-field' (Szabo & Ostlund 2012). The 'mean-field' is initially constructed from a 'guess', which is typically derived from the solution of Eq. (3.4) neglecting electron-electron interactions. The mean-field is subsequently used in constructing the 'Fock-operator'—the one-electron operator containing the electronic motion and (mean-field) Coulomb interactions—which is then inserted in the 'Roothaan'-equations to find a new wave function (Roothaan 1951). The associated energy of

the new wave function is guaranteed to be lower through the variational principle, and thus constitutes a 'better' solution to the system at hand. In this way, the wave function is iteratively updated until convergence is attained. The eventual wave function constitutes the 'Hartree-Fock' solution to Eq. (3.4).

Modern quantum chemical techniques exist to further improve the Hartree-Fock solution to the system. Techniques such as the coupled-cluster or configuration interaction method mitigate the error that has been introduced through the mean-field approximation (Bartlett & Musiał 2007). Full configuration interaction finds the 'exact' solution to Eq. (3.4) within a certain basis, but is generally very expensive. Coupled cluster techniques are usually considered to be the most cost-effective, but one compromises the variational principle with this technique.

The solution to Eq. (3.4) yields the 'electronic energy' and the 'electronic wave function' of the molecule. We note that the electronic energy is a function of the nuclear coordinates. The minimal electronic energy (as a function of the nuclear coordinates) defines the molecular geometry, or rather, the equilibrium coordinates. The electronic wave function defines how the (indistinguishable) electrons are distributed through the molecule according to the probability density. We will keep this in mind when we will consider the interactions between the electrons and external (and internally induced) magnetic fields.

3.1.2 Nuclear motion

We now return to the total molecular Hamiltonian that also includes the nuclear motion. Considering the nuclear motion to be far slower than electronic motions, we note

$$\begin{aligned}\hat{H} &= \hat{H}_{\text{nuc}} + \langle \hat{H}_{\text{el}}(\{\boldsymbol{r}_\alpha\})\rangle \\ &= \sum_\alpha \frac{\hat{p}_\alpha^2}{2m_\alpha} + V(\{\boldsymbol{r}_\alpha\}),\end{aligned} \tag{3.5}$$

where we note the nuclear kinetic energy in terms of momentum operators, $\hat{p}_\alpha$ and where we from now on will consider the electronic energy—that is a function of the nuclear coordinates—as a potential field through which the nuclei move. The nuclear coordinates associated with the minimal electronic energy we call the equilibrium coordinates and refer to these as $\{\boldsymbol{r}_\alpha^{(0)}\}$. We set the electronic potential energy at these points to zero. We furthermore define the coordinates $\{\boldsymbol{r}_\alpha\}$ in terms of displacements from the equilibrium coordinates (Wilson et al. 1980)

$$\boldsymbol{r}_\alpha = \boldsymbol{r}_\alpha^{(0)} + \boldsymbol{d}_\alpha, \tag{3.6}$$

and we represent the potential energy by the first two terms of its Taylor-expansion, in accordance with the harmonic approximation,

$$V(\{\boldsymbol{r}_\alpha\}) \approx \frac{1}{2}\sum_{\alpha\beta} \boldsymbol{d}_\alpha \cdot \left.\frac{\partial^2 V}{\partial \boldsymbol{d}_\alpha \partial \boldsymbol{d}_\beta}\right|_{\boldsymbol{d}_\alpha=\boldsymbol{d}_\beta=0} \boldsymbol{d}_\beta, \tag{3.7}$$

where we have been able to set the first-order term to zero because $V(\{\boldsymbol{r}_\alpha^{(0)}\})$ is a minimum. We re-state the nuclear Hamiltonian in the harmonic approximation

$$\hat{H}_{\text{nuc}} = \sum_\alpha \frac{\hat{\boldsymbol{p}}_\alpha^2}{2m_\alpha} + \frac{1}{2}\sum_{\alpha\beta} \boldsymbol{d}_\alpha \cdot \left.\frac{\partial^2 V}{\partial \boldsymbol{d}_\alpha \partial \boldsymbol{d}_\beta}\right|_{\boldsymbol{d}_\alpha=\boldsymbol{d}_\beta=0} \boldsymbol{d}_\beta. \tag{3.8}$$

This Hamiltonian can be represented as a sum of uncoupled harmonic oscillators in the 'normal coordinate' system, $\{Q_i,\ i = 1, 2, \cdots, 3N_\alpha\}$, in which the second-order potential operator is diagonalized (Papousek & Aliev 1982)

$$\hat{H}_{\text{nuc}} = \sum_i \left(\hat{P}_i^2 + \lambda_i \hat{Q}_i^2\right), \tag{3.9}$$

where the terms λ_i are the eigenvalues of the harmonic potential matrix and they are related to the harmonic frequencies: $\omega_i = \lambda_i^2$, and the momentum operators are formulated with respect to the transformed coordinates (Papousek & Aliev 1982). The normal-coordinates correspond to vibrational modes: we give the vibrational modes of water with the associated harmonic frequencies in Fig. (3.1). The first six eigenvalues of the harmonic potential matrix are zero if the electronic potential is invariant under rotation and translation operations. The first three normal modes can be set to zero by requiring

$$\sum_\alpha m_\alpha \boldsymbol{r}_\alpha = 0, \tag{3.10a}$$

which corresponds to using a center of mass frame; the first three modes thus correspond to the translational modes. The next three normal modes are the rotational modes and are set to zero by requiring

$$\sum_\alpha m_\alpha \boldsymbol{r}_\alpha^{(0)} \times \boldsymbol{d}_\alpha = 0. \tag{3.10b}$$

Equations 3.10 define an axis system in which coupling between translational and vibrational motion is removed, and coupling between rotation and vibration is minimized. The conditions of Eqs. (3.10) are the Eckart conditions (Eckart 1935).

We return to the nuclear Hamiltonian of Eq. (3.9) and discard the translation and rotation modes for the moment to be left with the vibrational Hamiltonian. In the 'normal coordinate' system, we recognize that the vibrational Hamiltonian

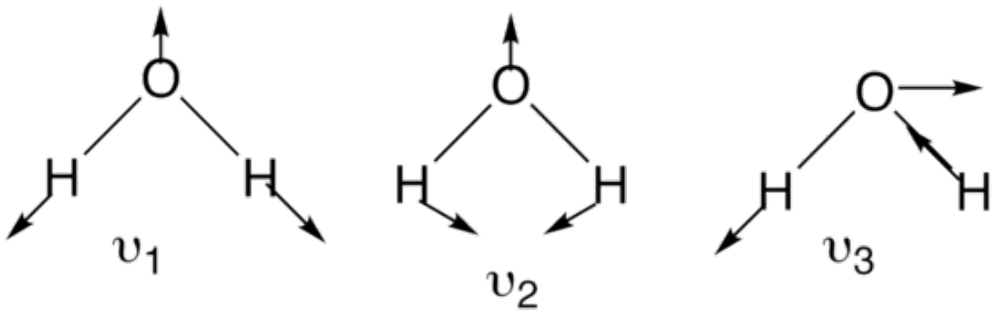

Figure 3.1: Vibrational normal modes of water. Mode v_1 (Q_1) corresponds to the symmetric stretch and has an harmonic frequency of 3657 cm^{-1}, v_2 (Q_2) corresponds to the symmetric bend and has an harmonic frequency of $\sim$ 1595 cm^{-1} and v_3 (Q_3) corresponds to the symmetric bend and has an harmonic frequency of $\sim$ 3756 cm^{-1}.

is the sum of $3N_\alpha - 6$[1] (uncoupled) quantum harmonic oscillator Hamiltonians

$$\hat{H}_i = \hat{P}_i^2 + \sqrt{\omega_i}\hat{Q}_i^2, \tag{3.11}$$

that have associated eigenvalues, $\hbar\omega_i(v_i + \frac{1}{2})$, dependent on the vibrational quantum number, v_i of mode i. Eigenfunctions are the Hermite functions of the normal coordinates. When higher-order terms of the electronic potential, $V(\{\boldsymbol{r}_\alpha\})$ are reintroduced, coupling between the normal modes will be present.

Vibrationally excited states and transitions will be important later in analyzing the alignment of molecules because they provide strong alignment potential for molecules close to strong sources of radiation. Also, when discerning molecular electromagnetic properties, it will be important to keep the internal motion of the nuclei in the electronic potential field in mind.

In our discussion of the vibrational structure of the molecule, we have considered the molecule to be stationary, and have captured all the rotational displacements in the normal modes 4 to 6. We will now investigate these modes as the proper rotation of the molecule. It will be too involved to start the derivation of the rotational Hamiltonian in a quantum-mechanical framework; but it will suffice for our purposes to consider rotational motion from a classical perspective. We will later refer to the proper way to transform the classical rotational Hamiltonian to a quantum-mechanical one.

The molecular rotation is not through an electronic potential field, and the energy consists only of the kinetic energy (Flygare 1978)

$$T_{\text{rot}} = \frac{1}{2}\sum_\alpha m_\alpha(\dot{\boldsymbol{r}}_\alpha)^2 \tag{3.12}$$

[1]A linear molecule has $3N_\alpha - 5$ vibrational modes, because rotation about the molecular axis cannot be observed.

of the rotation. We only take into account the motion of the nuclei as they carry nearly all of the molecules mass and thus kinetic energy. The velocity of a rotating object is $\dot{\boldsymbol{r}}_\alpha = \boldsymbol{\omega} \times \boldsymbol{r}_\alpha$, where $\boldsymbol{\omega}$ is the angular velocity. Using this relation in the expression for the rotational kinetic energy yields

$$T_{\text{rot}} = \frac{1}{2}\boldsymbol{\omega} \cdot \left[\sum_\alpha m_\alpha \left(r_\alpha^2 \mathbf{1} - \boldsymbol{r}_\alpha \otimes \boldsymbol{r}_\alpha\right)\right] \boldsymbol{\omega}, \tag{3.13}$$

where the part in brackets is commonly referred to as the inertiatensor: $\boldsymbol{I}$. The angular momentum, $\boldsymbol{J} = \frac{\partial T}{\partial \boldsymbol{\omega}}$, can be evaluated from the rotational kinetic energy, giving $\boldsymbol{J} = \boldsymbol{I}\boldsymbol{\omega}$, so that

$$T_{\text{rot}} = H_{\text{rot}} = \frac{1}{2}\boldsymbol{J} \cdot \boldsymbol{I}^{-1}\boldsymbol{J}.$$

The relation between this classical Hamiltonian and the quantum-mechanical one turns out to be trivial (Podolsky 1928)

$$\hat{H}_{\text{rot}} = \frac{1}{2}\hat{\boldsymbol{\mathcal{P}}} \cdot \boldsymbol{I}^{-1}\hat{\boldsymbol{\mathcal{P}}} = A\hat{\mathcal{P}}_a + B\hat{\mathcal{P}}_b + C\hat{\mathcal{P}}_c, \tag{3.14}$$

where $\hat{\boldsymbol{\mathcal{P}}}$ is the body-fixed angular momentum operator fulfilling the anomalous commutation relations (Brink & Satchler 1993). The constants $A = \frac{1}{2I_{aa}}$, $B = \frac{1}{2I_{bb}}$ and $C = \frac{1}{2I_{cc}}$ are the rotational constants and are defined with respect to the principal axis frame within which the inertia-tensor is diagonal and where the axes are chosen so that $A \geq B \geq C$ (Flygare 1978). The eigenfunctions of the angular momentum operators are

$$\hat{\boldsymbol{\mathcal{P}}}^2 |JKM\rangle = \hbar^2 J(J+1) |JKM\rangle, \tag{3.15a}$$

$$\hat{\boldsymbol{\mathcal{P}}}_a |JKM\rangle = \hbar K |JKM\rangle, \tag{3.15b}$$

where the operators fulfill the anomalous commutation relations (Brink & Satchler 1993). The quantum number M is associated with the space-fixed angular momentum operator, $\hat{\boldsymbol{\mathcal{J}}}$,

$$\hat{\boldsymbol{\mathcal{J}}}^2 |JKM\rangle = \hbar^2 J(J+1) |JKM\rangle, \tag{3.15c}$$

$$\hat{\boldsymbol{\mathcal{J}}}_a |JKM\rangle = \hbar M |JKM\rangle, \tag{3.15d}$$

whose operators fulfill the usual commutation relations (Brink & Satchler 1993). The space-fixed angular momentum operators will become important when the influence of external fields is considered. In the cases of very symmetrical molecules, $A = B = C$, and the eigenvalues to the rotational Hamiltonian (rotational energies) are simply

$$E_J = \hbar^2 BJ(J+1)$$

and the eigenfunctions $|JKM\rangle$ are degenerate for all K within J. These types of molecules are called spherical tops. It turns out that spherical tops share the energy-structure with linear molecules on the ground of negligible angular momentum along the interatomic axis. Molecules that have cylindrical symmetry have $A \neq B = C$ (prolate) or $A = B \neq C$ (oblate) are called symmetric tops and have rotational energies (here, only for a prolate)

$$E_{J|K|} = \hbar^2 B K^2 + \hbar^2 (A - B) J(J+1),$$

and the $|J(\pm K)M\rangle$ eigenstates are degenerate. Asymmetric tops, with $A \neq B \neq C$ have no good K quantum-number. Eigenfunctions and rotational energies have to be found by setting up $\hat{H}_{\rm rot}$ in a basis of Eq. (3.15) for a specific J (J is a good quantum number) and diagonalized. Diagonalization yields the eigenfunctions as a linear combination of $|JKM\rangle$ functions and the eigenvalues are the rotational energies. Eigenstates of asymmetric top molecules are usually denoted as J_{K_a,K_c}, referring to the projection on both the a (prolate) and c (oblate) projection axes.

At high rotational energies, centrifugal forces become important and start to affect the positions of the nuclei in the molecule. This has consequences for both the vibrational and the rotational structure, as equilibrium positions of the nuclei are altered. It is common to incorporate the effects of centrifugal (and other, such as Coriolis) forces as additional terms in a total Hamiltonian that depends on a lot of parameters. Such an extended Hamiltonian can be fitted to the observed spectrum of a particular molecule and return an accurate energy spectrum.

Concluding this section on the internal dynamics of molecules, we point out that internal torsional motion through a relatively weak potential field can influence the rotational dynamics of a molecule deeply (Lin & Swalen 1959). In this thesis, a lot of attention is dedicated to methanol, whose OH-group can rotate along the C−O-axis with respect to the CH_3-group through a relatively weak potential field, where the threefold torsional barrier is 373 $\rm cm^{-1}$ (Xu & Lovas 1997). When a molecule is torsionally active, the rotational dynamics cannot be considered in isolation from the internal nuclear motion and a rotation-torsion Hamiltonian has to be set-up and solved in order to properly model the rotational dynamics (Wilson et al. 1980). We perform such calculations in Paper I; where we study the electrodynamics and interactions with an external magnetic field of the torsionally active molecule methanol.

3.2 Molecular electrodynamics

In the previous section, we reviewed the internal dynamics of isolated molecules. The nuclei and electrons that make up the molecule are charged particles and their motion is therefore associated with electric and magnetic fields. In this section we review the electrodynamics relevant to the motion of charges in molecules. Both how it affects the energy structure, through (hyper)fine interactions and Zeeman effects, but also how different energy states can interact through a dipole moment that two states span.

3.2.1 Molecular electromagnetic properties

Molecular dipole moment

The nuclei and electrons that make up the molecule are all charged particles. If the charged particles are not evenly distributed, they yield multipole moments of the system. Classically, the dipole moment is given by (Jackson 1998)

$$\begin{aligned}\boldsymbol{\mu}(\boldsymbol{r}) &= \int d^3\boldsymbol{r}'\ \rho(\boldsymbol{r}')[\boldsymbol{r}-\boldsymbol{r}'] \\ &= \sum_{j}^{\text{all particles}} q_j(\boldsymbol{r}_j-\boldsymbol{r}),\end{aligned} \tag{3.16}$$

where $\rho(\boldsymbol{r})$ is the charge density at position $\boldsymbol{r}$ and we consider the particles, j, that make up the molecule as point particles with charge q_j. Earlier, we had already discussed that within the Born-Oppenheimer approximation, the nuclei are stationary with respect to the electron motion. With this in mind, we first compute the expectation value of the dipole moment with respect to the electronic motions

$$\begin{aligned}\boldsymbol{\mu}^{\text{el}}(\boldsymbol{r},\{\boldsymbol{r}_\alpha\}) &= e\sum_\alpha Z_\alpha(\boldsymbol{r}_\alpha-\boldsymbol{r}) - e\sum_j\int d^3\boldsymbol{r}_j\ |\psi_{\text{el}}(\boldsymbol{r},\{\boldsymbol{r}_\alpha\},\{\boldsymbol{r}_i\})|^2(\boldsymbol{r}_j-\boldsymbol{r}) \\ &= \langle\psi_{el}|\boldsymbol{\mu}(\boldsymbol{r})|\psi_{el}\rangle\,,\end{aligned} \tag{3.17}$$

where we denote the probability density function of the electron cloud by $|\psi_{\text{el}}|^2$. We recognize from Eq. (3.17) that for molecules such as homonuclear diatoms (H_2, O_2) or highly symmetric molecules such as CH_4, the dipole moment vanishes.

In formulating the molecular dipole moment, we have thus far assumed the nuclear-coordinates to be stationary and given. Indeed, the electronic dipole moment is a function of the nuclear coordinates: $\boldsymbol{\mu}^{\text{el}}(\{\boldsymbol{r}_\alpha\})$. In our discussion on the vibrational structure of molecules, we have seen that molecules vibrate around

the equilibrium configuration, $\{\boldsymbol{r}_\alpha^{(0)}\}$, along the vibrational normal modes. To obtain the dipole moment for a particular vibrational state, we thus have to weigh the dipole moment over the vibrational modes

$$\langle \boldsymbol{\mu}^{\mathrm{el}} \rangle_{v_1,v_2,\cdots v_n} = \int d^3\boldsymbol{r}_1 \int d^3\boldsymbol{r}_2 \cdots \int d^3\boldsymbol{r}_n |\Psi_{\mathrm{vib}}^{v_1,v_2,\cdots v_n}(\{\boldsymbol{r}_\alpha\})|^2 \boldsymbol{\mu}(\{\boldsymbol{r}_\alpha\}), \tag{3.18}$$

where $\Psi_{\mathrm{vib}}^{v_1,v_2,\cdots v_n}$ denotes the vibrational wave function of the $(v_1, v_2, \cdots v_n)$ vibrational state. The molecular dipole moment of the vibrational ground state will mostly have the character of the dipole moment at the equilibrium configuration.

Finally, we recognize that the molecule is rotating according to its associated rotational state: $|J_{K_a,K_c}\rangle$. Evaluating the dipole-operator for a specific rotational state,

$$\langle J_{K_a,K_c}| \langle \boldsymbol{\mu}^{\mathrm{el}} \rangle_{v_1,v_2,\cdots v_n} |J_{K_a,K_c}\rangle = 0, \tag{3.19}$$

it becomes clear that, indeed, molecules do not posses any dipole moment in a particular rovibronic state (Klemperer et al. 1993). It is only between different rovibronic states that molecules can posses a dipole moment. This will be an important insight when discussing the interaction of molecules with electromagnetic fields.

Molecular magnetic moment

The classical expression for a magnetic moment for a set of moving point charges is (Jackson 1998)

$$\begin{aligned} \boldsymbol{m} &= \frac{1}{2} \int d^3\boldsymbol{r}\ \boldsymbol{r} \times \boldsymbol{j}(\boldsymbol{r}) \\ &= \frac{1}{2} \sum_j q_j (\boldsymbol{r}_j \times \boldsymbol{v}_j). \end{aligned} \tag{3.20}$$

The magnetic moment is generated by the charged particles and their different motions. In the case of closed-shell molecules, the orbital currents from the electrons in the same orbit with counter-spin cancel each other out. Also, when we compare the vibrational motion to the rotational motion of the molecule, we recognize that the rotational motion is far greater, and thus the rotational contribution to the magnetic moment dwarfs the vibrational contribution (Moss & Perry 1973). For simplicity, we will assume in this discussion the molecule to be in the vibrational ground state, at the equilibrium geometry. If the motion of the molecule only comes from the molecular rotation: $\boldsymbol{v}_j = \boldsymbol{\omega} \times \boldsymbol{r}_j$, then

$$\begin{aligned} \boldsymbol{m} &= \frac{1}{2} \sum_j q_j \boldsymbol{r}_j \times \boldsymbol{\omega} \times \boldsymbol{r}_j \\ &= \mu_N \left[\frac{1}{\mu_N} \sum_j \frac{q_j}{2} \left(r_j^2 \mathbf{1} - \boldsymbol{r}_j \otimes \boldsymbol{r}_j \right) \boldsymbol{I}^{-1} \right] \boldsymbol{J}, \end{aligned} \tag{3.21}$$

where we used the relation between the angular velocity and the angular momentum, and consolidated the characteristically weighed charge distribution of the molecule in the dimensionless rotational g-tensor, $\boldsymbol{g}$, which is the entity between brackets. The charged particles that make up the molecule all contribute to the magnetic moment, depending on their velocity and charge. Because the electron cloud and nuclear positions are not the same, this results in a net magnetic moment due to the molecular rotation. In a full quantum mechanical derivation of the rotational magnetic moment, one also takes into account the mixing in of paramagnetic electronic energy levels due to the rotation. This effect contributes to the total magnetic moment. For detailed calculations, see Flygare (1978) and Sauer (2011). Note that the magnetic moment can be non-zero for a single rotational state, but is also present between different rotational states.

Hyperfine structure

In the previous section we outlined how the motions of the charged particles that make up a molecule give rise to a magnetic moment. The magnetic moment from the molecular rotation was given at the centre-of-mass of the molecule. Besides this rotational magnetic moment, it is the case that some nuclei posses internal magnetic moments on account of their "nuclear spin". The magnetic moment of a nucleus, K is proportional to the nuclear spin, $\boldsymbol{I}_K$ and the 'nuclear g-factor', g_K:

$$\boldsymbol{m}_K = \mu_N g_K \boldsymbol{I}_K. \tag{3.22}$$

When we consider the interaction of a the rotational magnetic moment, $\boldsymbol{m}$, located at the origin, and the magnetic moment of a nucleus, $\boldsymbol{m}_K$ at position, $\boldsymbol{r}$, we have the Hamiltonian of this 'spin-rotation' interaction

$$\begin{aligned} H_K^{SR} &= -\frac{\mu_0}{4\pi r^3}\left[3(\boldsymbol{m}_K \cdot \hat{\boldsymbol{r}})(\hat{\boldsymbol{r}} \cdot \boldsymbol{m}) - \boldsymbol{m}_K \cdot \boldsymbol{m}\right] \\ &= \boldsymbol{I}_K \cdot \left[\frac{\mu_0 \mu_N^2 g_K}{4\pi r^3}\left(\mathbf{1} - 3\hat{\boldsymbol{r}} \otimes \hat{\boldsymbol{r}}\right)\boldsymbol{g}\right]\boldsymbol{J} \\ &= \boldsymbol{I}_K \cdot \boldsymbol{M}_K \boldsymbol{J}, \end{aligned} \tag{3.23}$$

where μ_0 stands for the magnetic constant. As before, we contained the interactions in a tensor which is called the spin-rotation tensor, $\boldsymbol{M}_K$.

It should be noted that in our (semi-)classical model of the spin-rotation interaction, the spin-rotation tensor in our formulation does not fully capture the quantum mechanical intricacies of the spin-rotation interactions. More detailed derivations are given in (Sauer 2011) and (Flygare 1978), where special attention is given to the quantum chemical methodology behind computing this tensor from the electronic structure. For our discussion, it is sufficient to note that the nuclear-spin magnetic moment interacts with the molecular rotation via a rank-2 tensor, which

is calculable from ab-initio methods. The classical expressions for the nuclear-spin and the rotational angular momentum we have employed so far, can be shown to transform to their quantum-mechanical counterparts: $\boldsymbol{I}_K \rightarrow \hat{\boldsymbol{I}}_K$, $\boldsymbol{J} \rightarrow \hat{\boldsymbol{\mathcal{J}}}$. The total spin-rotation interaction Hamiltonian is obtained by summing the spin-rotation interaction of all nuclei, K, that have non-zero nuclear spin

$$\hat{H}_{SR} = \sum_K \hat{\boldsymbol{I}}_K \cdot \boldsymbol{M}_K \hat{\boldsymbol{\mathcal{J}}}. \tag{3.24}$$

If there are multiple nuclei with nuclear spin, K and L, which are separated by $\boldsymbol{r}_{KL} = \boldsymbol{r}_K - \boldsymbol{r}_L$, then the energy of the interaction of these magnetic moments is

$$\begin{aligned}
\hat{H}^{SS}_{KL} &= -\frac{\mu_0}{4\pi r^3_{KL}} \left[3(\boldsymbol{m}_K \cdot \hat{\boldsymbol{r}}_{KL})(\hat{\boldsymbol{r}}_{KL} \cdot \boldsymbol{m}_L) - \boldsymbol{m}_K \cdot \boldsymbol{m}_L\right] \\
&= \hat{\boldsymbol{I}}_K \cdot \left[\frac{\mu_0 \mu_N^2 g_K g_L}{4\pi r^3_{KL}} \left(\mathbf{1} - 3\hat{\boldsymbol{r}}_{KL} \otimes \hat{\boldsymbol{r}}_{KL}\right)\right] \hat{\boldsymbol{I}}_L \\
&= \hat{\boldsymbol{I}}_K \cdot \boldsymbol{D}_{KL} \hat{\boldsymbol{I}}_L.
\end{aligned} \tag{3.25}$$

It can be shown that the spin-spin interaction tensor, $\boldsymbol{D}_{KL}$, is a traceless tensor with only irreducible rank-2 components.

A third hyperfine interaction for closed-shell molecules is only present for nuclei with nuclear spin $I \geq 1$, which we denote as K', and is called the quadrupole interaction

$$\hat{H}_Q = \sum_{K'} \hat{\boldsymbol{I}}_{K'} \cdot \boldsymbol{Q}_{K'} \hat{\boldsymbol{I}}_{K'}. \tag{3.26}$$

Quadrupole interactions arise on account of the electric field gradient at the nucleus. They are often an order of magnitude stronger than spin-rotation and spin-spin interactions and dominate the hyperfine structure of a molecule like HCN to such an extent that astronomers frequently ignore its hyperfine interactions involving the H-atom.

The quadrupole, spin-rotation and spin-spin interactions make up the hyperfine Hamiltonian

$$\hat{H}_{\text{hyp}} = \hat{H}_Q + \hat{H}_{SR} + \hat{H}_{SS}, \tag{3.27}$$

and have to be added to the total molecular Hamiltonian to obtain its proper energy. Because hyperfine interaction energies are dwarfed even by rotational energies, it is common to consider the hyperfine Hamiltonian as a perturbation on the rotational structure of the molecule. To obtain matrix-elements of $\hat{H}_{\text{hyp}}$, rotational eigenfunctions, $|J_{K_a,K_c}\rangle$, have to be expanded with the nuclear-spin wave functions: $|I_1 M_1\rangle\,|I_2 M_2\rangle \cdots |I_N M_N\rangle$. Usually, the rotation-hyperfine wave function is kept tractable by utilizing symmetry properties of the molecule and angular momentum techniques.

3.2.2 Interaction of molecules with external fields

We have discussed the electronic, vibrational and rotational structure of the molecule and have laid out how electromagnetic interactions arise as a consequence of this structure. An electric dipole moment arises through an asymmetric distribution of charges, and magnetic moments arise through the differential rotation velocities of the charged particles that make up the molecule. We have studied the internal electromagnetic interactions, but now we will study how electric dipole moments and magnetic dipole moments interact with external electric and magnetic fields.

Magnetic fields

We have seen earlier that the differential motion of the charged particles that make up a molecule introduces a magnetic moment which is proportional to its rotational angular momentum

$$\hat{\boldsymbol{m}}_{\mathrm{rot}} = \mu_N \boldsymbol{g} \hat{\boldsymbol{\mathcal{J}}}, \tag{3.28}$$

where $\boldsymbol{g}$ is the so called rotational g-tensor, and $\hat{\boldsymbol{\mathcal{J}}}$ the rotational angular momentum. Additionally, the nuclei with nuclear spin possess an intrinsic magnetic moment

$$\hat{\boldsymbol{m}}_{\mathrm{I}} = \mu_N \sum_K g_K \hat{\boldsymbol{I}}_K, \tag{3.29}$$

where the sum over K runs over all nuclei with non-zero nuclear spin, g_K is the associated nuclear g-factor and $\hat{\boldsymbol{I}}_K$ nuclear spin angular momentum. The rotational and nuclear-spin magnetic momenta make up the total magnetic moment of a closed-shell molecule. These are commonly known as non-paramagnetic molecules. Molecules that have unpaired electrons, paramagnetic molecules, possess additional magnetic momenta due to electron spin and electronic orbital momentum. The electronic magnetic momenta are proportional to the Bohr magneton and are accordingly 3 orders of magnitude stronger than non-paramagnetic momenta (Brown & Carrington 2003).

An external magnetic field interacts with the magnetic moment as (Flygare 1978)

$$\hat{H}_B = \hat{H}_{BR} + \hat{H}_{BI} = -\hat{\boldsymbol{m}}_{\mathrm{rot}} \cdot \boldsymbol{B} - \hat{\boldsymbol{m}}_{\mathrm{I}} \cdot \boldsymbol{B}, \tag{3.30}$$

giving rise to the rotational and nuclear spin Zeeman effects. Under astrophysical conditions relevant to molecular radio and (sub)millimeter astronomy, Zeeman interactions ($\sim$ kHz/G) are way smaller than rotational interactions ($\sim$ 100 GHz). Since furthermore the external magnetic field is constant and non-oscillatory, we

only need to bother with perturbative elements. For the rotational Zeeman interactions, these are

$$\begin{aligned}\langle jm|\hat{H}_{BR}|jm'\rangle &= \mu_N||g||\,\langle jm|\boldsymbol{B}\cdot\hat{\boldsymbol{\mathcal{J}}}|jm'\rangle \\ &= \mu_N||g||Bm\delta_{mm'},\end{aligned} \tag{3.31}$$

if we choose the magnetic sublevels to be oriented with respect to the magnetic field direction. The reduced g-tensor, $||g||$, is a constant in the case we are dealing with a linear molecule or spherical top, but is specific to the rotational state for asymmetric tops: $||g|| = g_{j_{k_a,k_c}}$. The matrix-elements of the nuclear spin Zeeman effects have to be taken in a basis which is extended with the nuclear spin wave functions $|i_K m_K\rangle$.

An interesting and useful manifestation of the Zeeman effect in (astrophysical) spectra of molecular lines is through the spectral decoupling of right- and left-circularly polarized radiation. Radiative transitions between two states may be associated with a change in magnetic quantum number of $\Delta m = 0$, which are the π^0 transitions and are linearly polarized, or $\Delta m = \pm 1$, which are the $\sigma^{\pm}$ transitions and are left- and right-handedly circularly polarized. For a transition between two rotational levels, $|j_1 m_1\rangle$ and $|j_2 m_2\rangle$, with associated rotational g-factors g_1 and g_2, we have the transition frequency

$$\omega(j_1, m_1; j_2, m_2) = \omega_0 - \frac{\mu_N}{\hbar}\left[g_1 m_1 - g_2 m_2\right], \tag{3.32}$$

slightly displaced from the line-centre, ω_0, by the Zeeman-shifts. The average (weighed over the line-strengths) displacement of the circularly polarized transitions is (Degl'Innocenti & Landolfi 2006)

$$\Delta\omega(\sigma^{\pm}) = \pm\frac{\mu_N}{\hbar}\bar{g}B, \tag{3.33}$$

where

$$\bar{g} = \frac{g_1 + g_2}{2} + \frac{g_1 - g_2}{4}\left[j_1(j_1+1) - j_2(j_2+1)\right];$$

so for diatomic molecules simply $\bar{g} = g$. The circular polarization of the radiation is given in the Stokes-V profile. We give an example of a Zeeman-splitted spectral line in Fig. (3.2). The maximum polarization fraction of the Stokes-V profile can be analytically evaluated to be

$$p_V^{\max}(\%) \simeq 0.33\ \bar{g}\left(\frac{\Delta v_{\rm FWHM}}{1\ \rm km/s}\right)^{-1}\left(\frac{\nu_0}{100\ \rm GHz}\right)^{-1}\left(\frac{B}{1\ \rm G}\right), \tag{3.34}$$

for non-paramagnetic molecules, while it is

$$p_V^{\max}(\%) \simeq 0.61\ \bar{g}\left(\frac{\Delta v_{\rm FWHM}}{1\ \rm km/s}\right)^{-1}\left(\frac{\nu_0}{100\ \rm GHz}\right)^{-1}\left(\frac{B}{1\ \rm mG}\right), \tag{3.35}$$

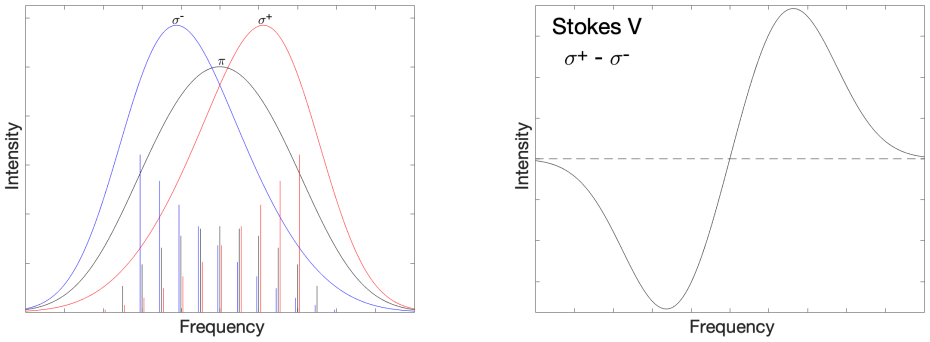

(a) (b)

Figure 3.2: Spectral decoupling of the different type of transitions ($\sigma^{\pm}$ and π). We have plotted the σ^{+}- (red), σ^{-}- (blue) and π- (black) -transitions within a $j = 5 \rightarrow j' = 6$-transition, with a certain Zeeman splitting, that is smaller than the (Gaussian) broadening of the line. Straight lines in the figure demarcate the individual $m \rightarrow m'$-transitions. The different $\sigma^{\pm}$ and π-transitions are spectrally decoupled, depending on the strength of the Zeeman effect. $\sigma^{\pm}$-transitions show an asymmetric spectrum, but do note that the total intensity, $\sigma^{+} + \sigma^{-}$, is symmetric.

for paramagnetic molecules. The maximum polarization fraction estimate is accurate up to polarization fractions of $\sim 10\%$. The transition g-factor, $\bar{g}$, generally takes the value of ~ 0.1. Indeed, as we can infer from Eq. (3.34), it is difficult to observe the Zeeman splitting of non-paramagnetic spectral lines directly. Only masers, with their extreme brightness and narrow velocity profiles present us with Zeeman profiles that are within the observational sensitivity limits. But, for thermal line-emission, non-paramagnetic Zeeman effects are unobservable under regular astrophysical conditions. Zeeman effects in non-paramagnetic molecules will however manifest through other secondary effects, as they force the molecule to precess along the magnetic field axis, and therefore endow it with a preferred orientation (Degl'Innocenti & Landolfi 2006; Goldreich & Kylafis 1981). In the next section, we will see how that can lead to the partial linear polarization of radiation that emerges from such molecules.

Electromagnetic radiation

In the following, we consider the interaction of electromagnetic (EM) radiation with a molecule. The interaction is dominated by the interaction of the oscillating electric field and the dipole moment; interactions between the oscillating magnetic field and the magnetic moment are some orders of magnitude weaker and are generally ignored.

We have already seen that the dipole moment of a certain molecular state

is zero. Indeed, only dipole moments *between* states are non-zero. Conversely, the electric field of EM radiation is oscillatory. Both these properties result in that dipole-EM radiation interactions result in a transition between two states, provided the transition dipole moment is non-zero and the radiation is resonant with the transition frequency.

The dipole moment and the EM-wave are both vectors, but the direction-dependent properties of their interaction are often ignored. Because we are particularly interested in directional properties through the alignment of molecules and polarization of radiation, we dedicate extra attention to it. We consider a transition between two molecular rotational levels $j_1 = 0 \rightarrow j_2 = 1$, where the magnetic sublevels are oriented along the magnetic field, $\boldsymbol{B}$. This molecule is interacting with the electric field part of an EM wave (see chapter 2)

$$\boldsymbol{E}(\boldsymbol{r}, t) = \mathrm{Re}\left(\tilde{\mathcal{E}}_+ e^{i\boldsymbol{k}\cdot\boldsymbol{r}-i\omega t}\hat{\boldsymbol{e}}_+ + \tilde{\mathcal{E}}_- e^{i\boldsymbol{k}\cdot\boldsymbol{r}-i\omega t}\hat{\boldsymbol{e}}_-\right), \tag{3.36}$$

where $\boldsymbol{k}$ is the EM-wave number and direction, and $\hat{\boldsymbol{e}}_\pm$ are the unit polarization directions, $\hat{\boldsymbol{e}}_\pm = \mp\frac{1}{\sqrt{2}}\left(\hat{\boldsymbol{e}}_\parallel \pm i\hat{\boldsymbol{e}}_\perp\right)$, chosen with respect to parallel and perpendicular projected magnetic field directions on the plane of the sky. The complex amplitude of the electric field part of the EM-wave is given by $\tilde{\mathcal{E}}_\pm$, and is oscillating with a frequency ω. The interaction between the electric field and the dipole moment, placed at $\boldsymbol{r} = 0$, is

$$\begin{aligned}\hat{V}(t) &= -\boldsymbol{E}(t)\cdot\hat{\boldsymbol{\mu}} \\ &= \frac{1}{2}\left[\tilde{\mathcal{E}}_-^* e^{i\omega t} + \tilde{\mathcal{E}}_- e^{-i\omega t}\right]\hat{\mu}_+ + \frac{1}{2}\left[\tilde{\mathcal{E}}_+^* e^{i\omega t} + \tilde{\mathcal{E}}_+ e^{-i\omega t}\right]\hat{\mu}_-.\end{aligned} \tag{3.37}$$

Now, we consider the transition rate from the ground state level, $|j_1 m_1\rangle = |00\rangle$, to an excited state level, $|j_2 m_2\rangle = |1m\rangle$, where $m = 0$ or $m = \pm 1$ and the transition frequency is ω_0. States are denoted by their total angular momentum j and magnetic sublevel m. To compute the transition rate from an oscillatory perturbation as Eq. (3.37), we use Fermi's Golden rule

$$\Gamma_m = \frac{2\pi}{\hbar^2}|\left\langle 1m|\tilde{\mathcal{E}}_-^*\mu_+ + \tilde{\mathcal{E}}_+^*\mu_-|00\right\rangle|^2\delta(\omega-\omega_0), \tag{3.38}$$

where we have invoked the rotating wave approximation and set the fast-rotating (2ω) elements zero.

Before working out the matrix elements of Eq. (3.38), we should linger on the elements $\mu_\pm$ of the dipole moment. We note that these elements arose out of the in-product with the electric field; and thus refer to an axis system related to the radiation direction. This is in contrast to the eigenfunctions, $|jm\rangle$ of the transition levels, which are related to the magnetic field direction. Thus, when we consider the matrix elements, we have to first rotate these elements back from the

radiation field frame (RF) to the magnetic field frame (MF)

$$\mu_{\pm}^{\rm RF} = \sum_m D^{(1)}_{\pm m}(\chi\theta\phi)\mu_m^{\rm MF}, \tag{3.39}$$

where $D^{(1)}_{qm}(\chi\theta\phi)$ is the Wigner D-matrix element for a rotation described by the Euler angles, $(\chi\theta\phi)$, that relate the propagation direction and the magnetic field direction. After rotating the dipole-vector to the proper frame, we can take the matrix elements

$$\langle 1m|\mu_{m'}^{\rm MF}|00\rangle = \frac{||\mu||}{\sqrt{3}} C^{0\ 1\ 1}_{0\ m'\ m}, \tag{3.40}$$

which are only non-zero for $m' = m$. In Eq. (3.40) we used the Wigner-Eckart theorem in the Racah-Wigner convention (Racah 1942; Wigner 1951) and $C^{j\ j'\ j''}_{m\ m'\ m''}$ represents a Clebsch-Gordan coefficient. Putting Eqs. (3.39) and (3.40) together we obtain for the dipole matrix-elements (Deguchi & Watson 1990)

$$\langle 10|\mu_{\pm}^{\rm RF}|00\rangle = \pm||\mu||\frac{1 \pm \cos\theta}{2\sqrt{3}}, \tag{3.41a}$$

$$\langle 11|\mu_{\pm}^{\rm RF}|00\rangle = i||\mu||\frac{\sin\theta}{\sqrt{6}}, \tag{3.41b}$$

both of which are dependent on the angle between the magnetic field and the radiation: $\cos\theta = \hat{\boldsymbol{k}} \cdot \hat{\boldsymbol{b}}$. Using Eqs. (3.41) in Eq. (3.38), we find the rates of absorption to $m = 0$ and $m = 1$ to be

$$\Gamma_0 = B_{j_1\to j_2} \sin^2\theta \frac{I+Q}{2}\delta(\omega - \omega_0), \tag{3.42a}$$

$$\Gamma_1 = \frac{B_{j_1\to j_2}}{2}\left(\frac{I-Q}{2} + \frac{I+Q}{2}\cos^2\theta\right)\delta(\omega - \omega_0), \tag{3.42b}$$

where we defined $B_{j_1\to j_2} = \frac{8\pi^2||\mu||}{3\hbar^2 c(2j_2+1)}$ as the Einstein B-coefficient of absorption and we can relate the Stokes parameters I and Q to the electric field amplitudes as

$$I = \frac{c}{8\pi}\left(\tilde{\mathcal{E}}_+^*\tilde{\mathcal{E}}_+ + \tilde{\mathcal{E}}_-^*\tilde{\mathcal{E}}_-\right), \tag{3.43a}$$

$$Q = \frac{c}{8\pi}\left(\tilde{\mathcal{E}}_+^*\tilde{\mathcal{E}}_- + \tilde{\mathcal{E}}_-^*\tilde{\mathcal{E}}_+\right). \tag{3.43b}$$

If we now generalize these absorption rates to astrophysical conditions, where radiation can come from any direction, Ω, and where the molecular absorbers are distributed over a velocity profile, ϕ_ν, we note the rate of absorption from $|00\rangle$ to $|10\rangle$ and $|1 \pm 1\rangle$ as (Goldreich & Kylafis 1981)

$$R_0 = B_{j_1\to j_2}\int d\nu\ \phi_\nu \int \frac{d\Omega}{4\pi}\ \sin^2\theta I_\parallel(\nu,\Omega), \tag{3.44a}$$

$$R_\pm = \frac{B_{j_1\to j_2}}{2}\int d\nu\ \phi_\nu \int \frac{d\Omega}{4\pi}\left(I_\perp(\nu,\Omega) + I_\parallel(\nu,\Omega)\cos^2\theta\right), \tag{3.44b}$$

where we defined $I_{\parallel,\perp} = (I \pm Q)/2$ as the radiation parallel and perpendicular to the magnetic field direction projected on the plane of the sky. One should make particular note, that the total rate of absorption from $j_1 \to j_2$,

$$R = R_- + R_0 + R_+ = B_{j_1 \to j_2} \int d\nu \phi_\nu \int \frac{d\Omega}{4\pi} \, I(\nu, \Omega) \tag{3.45}$$

has no particular weighing with respect to the incoming radiation direction. Thus, it is only the relative alignment of the molecular states that is a function of the anisotropic illumination of the molecules.

Suppose we consider the case that unidirectional unpolarized light, that is directed with an angle Θ with respect to the magnetic field, is shone on an ensemble of molecules at the transition frequency of the $0 \to 1$ transition. Now, the absorption rate of the $|00\rangle \to |10\rangle$, R_0, will be different to the absorption rate to the $|00\rangle \to |1 \pm 1\rangle$ transitions:

$$\frac{R_0}{R} = \frac{\sin^2 \Theta}{2}, \tag{3.46a}$$

$$\frac{R_\pm}{R} = \frac{1 + \cos^2 \Theta}{4}, \tag{3.46b}$$

and thus will result in the differential population of the $m = 0$ and $m = \pm 1$ levels of the $j = 1$ state. In practice, this means that the molecular states are partially aligned, as the differential population of the magnetic sublevels translates to a propensity to be found in some preferred direction with respect to the magnetic field. In the following section, we give an intuitive introduction to molecular alignment by connecting it to a classical picture of alignment. This will prepare us for the next chapter, where we consider the interaction of radiation and molecules—and its relation to the alignment of molecules under astrophysical conditions—in more detail.

3.3 Modeling the alignment of molecules

Alignment is said to be present when the molecules have propensity to be found in some preferred direction. In this section, we lay briefly a connection between the classical description of alignment, and its representation for a quantized rotational level. The quantum mechanical representation becomes equivalent to the classical description for rotational angular momentum $j \to \infty$. Because of their attractive symmetry properties, we represent the alignment properties of molecules in terms of irreducible tensor elements.

First, we consider a collection of N classical molecules under the influence of a

magnetic field. Due to the magnetic field, the molecule precesses around the magnetic field axis with a rate of $\sim s^{-1}$ for a mG magnetic field. Under ISM conditions, the precession rate is therefore far greater than any other interaction rate, so after each interaction event, the molecule will re-orient itself with respect to the magnetic field axis and precess around it with an angle θ. We will find $n(\theta)d\theta$ molecules precessing with an angle, θ, around the magnetic field axis. We can expand $n(\theta)$ in terms of Legendre polynomials

$$n(\theta) = n_0 P_0(\cos\theta) + n_1 P_1(\cos\theta) + n_2 P_2(\cos\theta) + \cdots . \tag{3.47}$$

Using the orthogonality of the Legendre polynomials, the elements n_k are

$$n_k = \frac{[k]}{2} \int_{-1}^{1} d\cos\theta \; n(\theta) P_k(\cos\theta), \tag{3.48}$$

where $[k]$ is a short-hand notation for $2k+1$. It is easy to see that $n_0 = N$, the total number of molecules. The other elements that have $k =$ uneven are related to the orientation of the molecules, while the $k =$ even populations are related to the alignment (Blum 1981). We proceed to introduce the notation of orientations and alignments in terms of irreducible tensor elements. It is convenient to work in terms of irreducible tensor elements, because of the symmetry properties and convenient rotation properties of these elements.

We note the irreducible tensor element, ρ_q^k, of rank-k and projection q. In this introduction we are only interested in the case of a strong magnetic field, where only the $q = 0$ term survives, as the $q \neq 0$ terms average out to 0 due to the fast magnetic precession. The irreducible tensor elements are related to the expansion elements n_k by (Blum 1981)

$$\rho_0^k(j \to \infty) = \frac{1}{\sqrt{4\pi[k]}} n_k. \tag{3.49}$$

We note that in the distribution $n(\theta)$ we have assumed a continuum of states that can adopt the orientation, θ. This is akin to assuming a 'classical distribution' of the angular momentum vectors. The assumption of classical rotation becomes exact when $j \to \infty$. For smaller, finite, j, quantum effects play a role and this has to be accounted for in the representation of the irreducible tensor elements. The quantum states of a rotating molecule are $|jm\rangle$ (see section 3.1). The probability of finding part of the N molecules in the $|jm\rangle$ state is obtained by taking the matrix element over the density operator, $\hat{\rho}$,

$$\rho_{mm}(j) = \langle jm|\hat{\rho}|jm\rangle \, . \tag{3.50}$$

Off diagonal elements of the density-matrix, $\langle jm|\hat{\rho}|jm'\rangle$, are called coherence elements. In analogy to the classical case, for a molecule in a strong magnetic field,

only the diagonal $\rho_{mm}(j)$ elements are non-zero (it is exceedingly likely to find a molecule precessing with respect to the magnetic field). The quantum-state irreducible tensor elements of rank k and projection q, are defined as

$$\rho^k_q(j) = \sum_{mm'} (-1)^{j-m} [k]^{1/2} \begin{pmatrix} j & j & k \\ m & -m' & q \end{pmatrix} \rho_{mm'}(j), \tag{3.51}$$

where the entity demarcated by round brackets is called a Wigner 3j-symbol. Comparing the orientation ρ^1_0 and the alignment ρ^2_0 for the classical and the quantum case

$$\rho^1_0(\infty) = \sqrt{\frac{3}{4\pi}} \int_{-1}^{1} d\cos\theta \; n(\theta) \cos\theta, \tag{3.52a}$$

$$\rho^1_0(j) = \sqrt{\frac{3}{[j]j(j+1)}} \sum_m m\rho_{mm}, \tag{3.52b}$$

$$\rho^2_0(\infty) = \sqrt{\frac{5}{4\pi}} \int_{-1}^{1} d\cos\theta \; n(\theta) \frac{3\cos^2\theta - 1}{2}, \tag{3.52c}$$

$$\rho^2_0(j) = \sqrt{\frac{5}{(2j+3)(j+1)(2j+1)j(j-1)}} \sum_m [3m^2 - j(j+1)]\rho_{mm}. \tag{3.52d}$$

In particular, note the relation between the projection quantum number, m, normalized with the length of the angular momentum vector, $\sqrt{j(j+1)}$, to the projection on the magnetic axis, $\cos\theta$, in the classical description. In the classical limit, $2j+1 \to 4\pi$, which makes that in the limit of $j \to \infty$, these two descriptions converge.

Next chapter, we make thankful use of the formalism of molecular density states in terms of their irreducible tensor elements. This is particularly useful when treating the generation of partially polarized radiation. Just as is the case for aligned dust, an ensemble of aligned molecules tend to emit partially polarized radiation.

Chapter 4

Light & Molecules

In the preceding chapters of this thesis we have studied the nuclear motion and electronic structure of molecules. We have seen how electric and magnetic fields can interact with these molecules and we reviewed some of the appropriate molecular physics required to conveniently compute the interaction terms. We have also studied the properties of light and dedicated particular attention to its polarization properties

In this chapter we combine these results from previous chapters and study the interaction of light with molecules. In particular, the interaction of radio to (sub)millimeter radiation with molecules in the ISM provides for an interesting problem, because in these regions, the radiative interactions are of the same order as the collisional interactions, making a comprehensive excitation analysis necessary.

An additional effect that significant radiative interactions have on the molecular populations, is that if the interacting radiation field is anisotropic, this results in the partial alignment of the interacting molecules. Already in the case of weak magnetic fields, this alignment is with respect to the magnetic field direction and results in polarized radiation signals that trace the magnetic field morphology of the region in which the molecules are excited.

In light of these observations, we discuss maser polarization and the GK effect. Maser polarization provides a simple system of dominant radiative interactions because of the effects of strong amplification of the radiation through stimulated emission processes. In terms of polarization analysis, its simple (approximately) one-dimensional geometry makes it a good system to analyze analytically. After our discussion of maser polarization, we move on to thermal line polarization through an anisotropic velocity gradient in the LVG approximation. We end this chapter by discussing the general full 3D radiative transfer and excitation modeling, and outline a method to incorporate this into an alignment and polarization analysis.

4.1 Molecular excitation analysis

The population of the energy-levels of molecules is determined by balancing the radiative and collisional excitations and de-excitations. In particular, in astrophysical regions, the rates of collisional and radiative interactions are often comparable. A comprehensive analysis needs to be made to evaluate the excitation of a particular molecule embedded in an astrophysical region. Because radiative interactions are important, this has to be done in conjunction with evaluating the transfer of radiation.

When a system is equilibrated with a heat bath of temperature, T, statistical mechanics tells us that the probability of finding the system in a state, i, with energy ϵ_i, is (Thorne & Blandford 2017)

$$p_i \propto e^{-\epsilon_i/kT}, \tag{4.1}$$

where k is known as the Boltzmann constant. Thus, the ratio of probabilities between two states, i and j,

$$\frac{p_j}{p_i} = e^{-\frac{\epsilon_j - \epsilon_i}{kT}} \tag{4.2}$$

depends only on the states' energy and the temperature. If we suppose that the system is an ensemble of molecules, with discrete energy levels, and that $\epsilon_j > \epsilon_i$, then Eq. (4.2) shows, that thermal equilibrium requires $p_j < p_i$; the upper energy level is less populated than the lower energy level.

It is rare for a system to be in thermal equilibrium in astrophysics. If we focus on the ISM, it is usually the low densities of these regions that make thermal equilibrium unattainable. Molecular gas in the ISM consists mostly of H_2 that acts as a heat bath. But under conditions of low densities, the coupling of a certain molecular species to the H_2 heat bath via collisions is weak. If a molecule, for instance CO, would be left to itself, it would gradually relax to its lowest energy configuration through the emission of radiation. Therefore, only when the rate of collisions with H_2 is much higher than the rate of radiative relaxation can thermal equilibrium be attained. Usually, however, in the ISM, radiative rates are of the order of the heat-exchanging collisions.

When we have to consider radiative effects as a feature of the molecular excitation, it is not only radiative relaxation we have to take into account. Indeed, when a molecule relaxes radiatively from state j to state i, this relaxation is associated with the emission of a photon of energy $(\epsilon_j - \epsilon_i)$. Obviously, this photon is resonant with the transition $j \to i$, and it is thus a possibility that this

photon is subsequently absorbed again by another molecule in the same region. Alternatively, the photon is lost to the (local) ensemble of molecules when it is not absorbed. Thus, to keep track of the energy-level population of a molecular ensemble, we have to model the transfer of radiation through the molecular ensemble in conjunction with the collisional coupling of it with the H_2 heat bath. We model the transfer of radiation of frequency, ν, close to the resonant frequency ν_{ij}, through a molecular medium using the radiative transfer equation (see also section 2.1)

$$\frac{d}{ds}I_\nu = -\kappa_\nu I_\nu + \epsilon_\nu, \tag{4.3}$$

where the opacity includes absorption and stimulated emission (Rybicki & Lightman 2008)

$$\kappa_\nu = \frac{h\nu}{4\pi}B_{ij}(n_i - \frac{g_j}{g_i}n_j)\phi_\nu, \tag{4.4}$$

where n_i and n_j are the number densities of the lower and upper level and g_i and g_j its degeneracies. The Einstein B-coefficient is B_{ij}, and is defined in Eq. (3.42). The line profile, ϕ_ν, is centered around the resonance frequency and usually takes the form of a Doppler profile

$$\phi_\nu = \frac{1}{\sqrt{\pi}b_\nu}e^{-\left[\frac{\nu-\nu_{ij}}{b_\nu}\right]^2}, \tag{4.5}$$

where b_ν is the Doppler b-parameter in frequency units. The emissivity of the medium is (Rybicki & Lightman 2008)

$$\epsilon_\nu = \frac{h\nu}{4\pi}A_{ji}n_j\phi_\nu, \tag{4.6}$$

where the Einstein A-coefficient, A_{ji}, is defined below. When the levels are Boltzmann distributed according to a certain temperature, T, the ratio $\epsilon_\nu/\kappa_\nu \rightarrow B_\nu(T)$ becomes the Planck function.

Returning to the interaction of molecular matter with radiation, we invoked three processes relevant to the molecular excitation and transfer of radiation: (i) spontaneous emission, where a molecule spontaneously relaxes from upper state j to lower state i, while emitting a photon of frequency $(\epsilon_j - \epsilon_i)/h$ in a random direction, (ii) absorption, where a molecule absorbs a photon of frequency $(\epsilon_j - \epsilon_i)/h$, while exciting the molecule from state i to state j, (iii) stimulated emission, where a molecule under the influence of a photon of frequency $(\epsilon_j - \epsilon_i)/h$ emits an additional such photon, in the same direction, while relaxing from upper state j to lower state i. The rate of spontaneous emission is only determined by molecular

properties, and is specific to the transition $j \rightarrow i$, and is denoted, A_{ji}. The symbol A_{ji} is the Einstein-A coefficient

$$R^{j\rightarrow i}_{\text{spont}} = A_{ji}.$$

The rate of absorption and the rate of stimulated emission are determined by molecular properties and the strength of the radiation field. The rate of absorption is

$$R^{i\rightarrow j}_{\text{abs}} = B_{ij}\bar{J}_{ij},$$

where B_{ij} is the Einstein-B coefficient of absorption and J_{ij} is specific intensity, integrated over all directions, and resonant with the $i \rightarrow j$ transition of the molecular ensemble

$$\bar{J}_{ij} = \int d\nu \int \frac{d\Omega}{4\pi}\, I_\nu \phi_\nu. \tag{4.7}$$

The rate of stimulated emission is

$$R^{j\rightarrow i}_{\text{stim}} = B_{ji}\bar{J}_{ij}$$

where B_{ji} is the Einstein-B coefficient of stimulated emission. Transitions between levels i and j due to inelastic collisions are denoted C_{ij}. Arguments of detailed balance relate collisional excitation and de-excitation rates by $C_{ij}/C_{ji} = \frac{g_i}{g_j} e^{-\frac{\epsilon_j - \epsilon_i}{kT}}$. We note the change in the population of level i as a function of radiative and collisional events (van der Tak et al. 2007)

$$\begin{aligned}
\dot{n}_i &= \sum_{j>i} \left[R^{j\rightarrow i}_{\text{spont}} + R^{j\rightarrow i}_{\text{stim}} + C_{ji}\right] n_j + \sum_{j<i} \left[R^{j\rightarrow i}_{\text{abs}} + C_{ji}\right] n_j \\
&\quad + n_i \sum_{j<i} \left[R^{i\rightarrow j}_{\text{spont}} + R^{i\rightarrow j}_{\text{stim}} + C_{ij}\right] + n_i \sum_{j>i} \left[R^{i\rightarrow j}_{\text{abs}} + C_{ij}\right] \\
&= \sum_{j\neq i} n_j P_{ji} - n_i \sum_{j\neq i} P_{ij}.
\end{aligned} \tag{4.8}$$

So that we can define

$$P_{ij} = \begin{cases} A_{ij} + B_{ij}\bar{J}_{ij} + C_{ij}, & \text{if } i > j \\ B_{ij}\bar{J}_{ij} + C_{ij}, & \text{if } j > i. \end{cases} \tag{4.9}$$

It is easy to see that when the collisional rates far exceed the radiative rates, i.e. when the coupling to the H_2 heat-bath is strong, we obtain Boltzmann distributed level number densities. When radiative rates are higher or in the order of collisional rates, we have to solve Eqs. (4.3) and (4.8) together. This is one of the main problems that radiative transfer models try to solve.

Suppose we want to determine the molecular excitation (here written as a vector with elements n_i), $\boldsymbol{n}(\boldsymbol{r})$ as a function of the position $\boldsymbol{r}$, given a certain model for the temperature $T(\boldsymbol{r})$, hydrogen number density, $n_{\mathrm{H}_2}(\boldsymbol{r})$, velocity structure $\boldsymbol{v}(\boldsymbol{r})$ and molecular abundance $x_{\mathrm{mol}}(\boldsymbol{r})$. The radiation field at a specific point $\boldsymbol{r}_0$, $I_\nu(\boldsymbol{r}_0, \Omega)$ is a function of the excitation, $\boldsymbol{n}(\boldsymbol{r})$, of the entire system, while the excitation at point $\boldsymbol{r}_0$, $\boldsymbol{n}(\boldsymbol{r}_0)$, is a function of the specific intensity at that point, because it determines the rates absorption and stimulated emission. Additionally, one has to consider the contribution of the co-spatial dust to the radiative transfer of Eq. (4.3). It may be clear that radiative problems can rapidly become prohibitively complex.

We will come back to solving the radiative transfer equations for complex physical systems in section 4.4. Before that, we comment on an approximation that reduces the complexity of the radiative transfer problem greatly: the Sobolev approximation (Sobolev 1957; Ossenkopf 1997). In the Sobolev approximation, we consider a system with a velocity gradient in direction $\hat{\boldsymbol{r}}$, $dv_{\hat{\boldsymbol{r}}}/ds = dv/ds$, which is the same in all directions. At a later stage, we consider the Sobolev approximation for a plane-parallel system. If a velocity gradient is present, the radiation that is resonant with a certain transition is confined to a region of the order of the Sobolev length

$$s_0 = \frac{b}{dv/ds}, \tag{4.10}$$

where b is the Doppler-b parameter, representing the width of a line in velocity-space. For strong gradients, we note that the Sobolev length is small. At small enough Sobolev lengths, we can consider the molecular excitation to be constant throughout the region characterized by the Sobolev length. The line-profile of a certain transition

$$\begin{aligned} \phi_v &= \frac{c}{\nu}\phi_\nu = \frac{1}{\sqrt{\pi}b} e^{-(v/b)^2} \\ &= \frac{1}{\sqrt{\pi}b} e^{-([dv/ds]s/b)^2}, \end{aligned} \tag{4.11}$$

can be related to the distance s along the line-of-sight. If we restate Eq. (4.3) by factorizing $\kappa_\nu = k_{ij}\phi_\nu$, we obtain

$$\frac{dI_\nu}{ds} = -k_{ij}\phi_\nu[I_\nu - S_\nu]. \tag{4.12}$$

The solution of this radiative transfer equation can be inserted into the expression

for $\bar{J}_{ij}$

$$\begin{aligned}\bar{J}_{ij} &= \int \frac{d\Omega}{4\pi} \int d\nu \phi_\nu I_\nu \\ &= \int \frac{d\Omega}{4\pi} \left[S_{ij} - (S_{ij} - I_{ij}^{(0)}) \frac{1 - e^{-\tau_{ij}}}{\tau_{ij}} \right], \end{aligned} \tag{4.13}$$

where $\tau_{ij} = \int ds \phi_\nu k_{ij} = c k_{ij} / \nu_{ij} (dv/ds)$ and $I_{ij}^{(0)}$ is the background radiation field for the $i \rightarrow j$ transition. It may be noted that $\bar{J}_{ij}$ has become a function of the populations of the number densities of the levels associated with the transition $i \rightarrow j$. Thus, by inserting $\bar{J}_{ij}(n_i, n_j)$ into the set of equations of Eq. (4.8), we are left with a problem of the type

$$\mathbf{0} = \boldsymbol{\mathcal{Q}}(\boldsymbol{n})\boldsymbol{n},$$

which can be solved using root-finding algorithms such as the Newton-Raphson method. It is worth noting that for high optical depths, the solution of Eq. (4.8) returns the Boltzmann distribution. This may be expected, because photons do not escape the Sobolev region in this limit. The excitation of molecules departs from simple Boltzmann statistics at low densities, where the collisional coupling to H_2 is weak, and finite optical depths, where the molecular ensemble is effectively 'cooled' through the loss of photons. The departure from Boltzmann statistics sometimes leads to a situation, where an upper level j is higher populated than a lower level i: population inversion. Population inversion gives rise to a 'negative opacity' (see Eq. (4.4)), which has profound effects on the radiative transfer: the molecule is said to be 'masing'.

4.2 Masers

A peculiar case of the interaction of radiation and matter occurs when the population of two states are inverted, the higher energy level is more populated than the lower energy level. When this is the case, we speak of masers. Masers are characterized by the exponential amplification of (resonant) radiation and a highly beamed (almost one-dimensional) geometry. The radiative transfer of such systems can be viably simplified, and they form the most basic systems where polarization of the radiation arises through the alignment of the molecular states by directional radiative interactions.

When the conditions are such that population inversion is produced between two (usually rotational) molecular energy levels, we speak of a MASER (Microwave Amplified by Stimulated Emission of Radiation). Maser refers to the radiative transfer, where the process of stimulated emission is more likely than absorption,

so that a resonant radiation field gets amplified instead of attenuated. In this section, we discuss briefly the radiative transfer of masers, including an important feature of the radiative transfer, namely 'maser beaming'. We will lay particular emphasis on a consequence of maser beaming, which we show to be the partial polarization of radiation.

4.2.1 Radiative transfer

Suppose we study a transition between upper level a and lower level b. We write out the rate of change of the a'th and the b'th level populations. In accordance to Eq. (4.8), we may note the rate of change as

$$\begin{aligned}\dot{n}_a &= \sum_{i\neq a,b} P_{ia} n_i - n_a \sum_{i\neq a,b} P_{ai} + n_b P_{ba} - n_a P_{ab} \\ &= \lambda_a - n_a\gamma_a + [B_{ba}\bar{J}_{ba} + C_{ba}]n_b - [A_{ab} + B_{ab}\bar{J}_{ab} + C_{ab}]n_a \qquad (4.14a)\\ \dot{n}_b &= \lambda_b - n_b\gamma_b - [B_{ba}\bar{J}_{ba} + C_{ba}]n_b + [A_{ab} + B_{ab}\bar{J}_{ab} + C_{ab}]n_a. \qquad (4.14b)\end{aligned}$$

We call all other levels that are not participating in the transition between a and b the 'reservoir'. Note that we have consolidated the radiative and collisional interactions with the reservoir in the pumping-rates: λ_a and λ_b, and the decay-rates: γ_a and γ_b. The decay rate of state a, γ_a, encapsulates all absorption and collisional excitations of state a to higher states, and all spontaneous and stimulated emissions, and collisional de-excitations, of state a to lower states. The pumping rate of state a, λ_a, includes all absorption and collisional excitations to state a from lower states to state a, and all spontaneous and stimulated emissions, and collisional de-excitations, from higher states to state a.

If we suppose that $\lambda_a/\gamma_a > \lambda_b/\gamma_b$, then the upper level is consistently higher populated than the lower $n_a > g_b n_b/g_a$. In this case of 'population inversion', we recognize in the radiative transfer equation, Eq. (4.3), that the rate of stimulated emission is higher than absorption. Because of this, the transition has a negative optical depth, and thus the radiative transfer is characterized by the exponential amplification of radiation.

Because of the exponential amplification of maser radiation, the radiation field will be mainly comprised of those maser-rays that have the longest coherent path-length. This effect is called maser beaming. For an interferometer observing a maser source, maser beaming means that only a fraction of the source is effectively visible: the maser appears a lot smaller than it actually is. A local effect of maser beaming is, if one follows the local radiation transfer in the maser cloud, that it is the rays with the longest path-length, that subtend a small solid angle, that dominate the local radiation field resonant with the maser transition. So we can approximate the radiation that interacts with the maser transition to be

approximately one-dimensional (Gray 2012; Elitzur 1992)

$$\bar{J}_{ab} = \Delta\Omega \int dv\ \phi_v I(\nu_{ij}[1 - v/c], \Omega_0), \tag{4.15}$$

where Ω_0 is the direction of the maser and $\Delta\Omega$ is the beaming angle. The symbol ϕ_v denotes the velocity-distribution for the maser-states. Because of the strong radiation field, the rates of absorption and stimulated emission for a maser-line are far greater than the spontaneous emission rate and the collision rate. We can therefore neglect the effects of spontaneous emission and collisions on the populations, and we arrive at the simplified evolution equations

$$\dot{n}_a = \lambda_a - n_a\gamma_a - B_{ab}\bar{J}_{ab}\left[n_a - \frac{g_a}{g_b}n_b\right], \tag{4.16a}$$

$$\dot{n}_b = \lambda_b - n_b\gamma_b + B_{ab}\bar{J}_{ab}\left[n_a - \frac{g_a}{g_b}n_b\right]. \tag{4.16b}$$

If the decay rates for the upper and lower level are the same $\gamma_a \simeq \gamma_b$, we can easily compute the population inversion, $\Delta n = n_a - g_a n_b/g_b$, under steady-state conditions as

$$\Delta n = \frac{\Delta\lambda}{\gamma + 2B_{ab}\bar{J}_{ab}} = \frac{\Delta n_0}{1 + \frac{\bar{J}_{ab}}{J_{\rm sat}}}, \tag{4.17}$$

where $\Delta n_0 = \Delta\lambda/\gamma$ is the population inversion at weak maser fields, and $J_{\rm sat} = \gamma/2B_{ab}$ is the saturation intensity.

The population (inversion) is a function of the velocity. The velocity distribution is taken to be a Doppler profile in the case of an unsaturated maser $\bar{J}_{ab} \ll J_{\rm sat}$, while under conditions of maser saturation, the profile will be affected by the radiation field. Similarly, the radiation spectrum quickly departs from the Doppler profile that characterizes thermal lines. Because of the exponential amplification of radiation, the spectrum is narrowed, as on-resonance radiation is amplified more strongly. In a rigorous analysis, the velocity-dependent population inversion and the frequency-dependent intensity are comprehensively analyzed. In this elementary derivation, we assume that the population inversion and the intensity assume rectangular profiles of width Δv and $\Delta\nu = \frac{\nu_0}{c}\Delta v$,

$$\Delta n(v) = \frac{\Delta n}{\Delta v}, \qquad \text{for } -\Delta v/2 \le v \ge \Delta v/2, \tag{4.18a}$$

$$I_\nu = I, \qquad \text{for } \nu_0 - \Delta\nu/2 \le \nu \ge \nu_0 + \Delta\nu/2. \tag{4.18b}$$

The radiative transfer can then be noted

$$\frac{d}{ds}I = \frac{h\nu_0}{4\pi}B_{ab}\Delta n I, \tag{4.19}$$

where we furthermore ignored the contribution of the spontaneous emission. The term for the population inversion can be related to the maser brightness using Eq. (4.17). The resonant radiation field interacting with the maser transition can be trivially evaluated from Eqs. (4.15) and (4.18): $\bar{J}_{ab} = \Delta\Omega I$. If we define the opacity at weak maser fields $\kappa_0 = \frac{h\nu_0}{4\pi} B_{ab} \Delta n_0$, then we can re-state the radiative transfer equation as

$$\left[1 + \frac{\Delta\Omega I}{J_{\rm sat}}\right] d\left(\ln I\right) = \kappa_0 ds. \tag{4.20}$$

It is interesting to consider this differential equation in the limits of weak, unsaturated masers, and the strong, saturated masers. For an unsaturated maser, where the maser brightness is weak compared to the saturation intensity, we note that the solution to Eq. (4.20) becomes

$$I = I_0 e^{\kappa_0 s}, \quad \text{for } \Delta\Omega I / J_{\rm sat} \to 0, \tag{4.21}$$

which is simply exponential growth of the maser intensity. As a result, the maser brightness will rapidly increase, and the maser will saturate. In the strongly saturated regime, the maser brightness temperature is far greater than the saturation intensity and the equation of radiative transfer

$$\frac{d\left(\Delta\Omega I\right)}{d\left(\kappa_0 s\right)} = J_{\rm sat}, \quad \text{for } \Delta\Omega I / J_{\rm sat} \gg 1 \tag{4.22}$$

is an equation describing linear growth of the maser intensity.

4.2.2 Maser polarization

In order for polarization to emerge in the maser radiation, we require the maser states to be partially aligned. Alignment is said to be present when the molecules have propensity to be found in some preferred direction.

In the coming derivation, we consider the interaction of the maser molecules with the magnetic field to be dominant: the magnetic field determines the symmetry axis of the molecules. This means that the magnetic precession rate, $g\Omega$ ($\sim$ s^{-1}/mG), is far higher than rates of stimulated emission, collisions, or spontaneous emission events. In the case of a dominant magnetic field, the molecule will have ample time to re-orient itself around the magnetic field after each (stimulated emission) interaction event. That means that the alignment of a single molecule can be described by only the angle its angular momentum vector makes with the magnetic field direction around which the molecule precesses (see also section 3.3). In paper II, we show the proper theory and modeling of maser polarization that relaxes the assumption of a dominant magnetic field.

Suppose we have a maser radiation field that is partially polarized. Just as before, we consider it to have a rectangular velocity profile, and that it is strongly

beamed. We let I be the total intensity of the radiation field on resonance with the maser transition $a \rightarrow b$, while Q is its polarized intensity. The polarized intensity is defined $Q = I_{\parallel} - I_{\perp}$: positive Q describes polarization parallel to the projected magnetic field direction. The angle that the propagation direction makes with the magnetic field is $\hat{\boldsymbol{k}} \cdot \hat{\boldsymbol{b}} = \cos\theta$. Because we are interested in describing the directional properties of both the radiation and the maser states, we use the irreducible tensor formalism that is introduced in section 3.3. The relevant radiation field irreducible tensor elements are (Degl'Innocenti & Landolfi 2006)

$$\begin{aligned}\bar{J}^0_0 &= \int d\nu\ \phi_\nu \int d\Omega'\ I(\nu,\Omega') \\ &= \Delta\Omega I = \bar{J}_{ab}, \end{aligned} \tag{4.23a}$$

$$\begin{aligned}\bar{J}^2_0 &= \int d\nu\ \phi_\nu \int d\Omega'\ \left[\frac{3\cos^2\theta' - 1}{2\sqrt{2}} I(\nu,\Omega') - \frac{3\sin^2\theta'}{2\sqrt{2}} Q(\nu,\Omega')\right] \\ &= \Delta\Omega \left[\frac{3\cos^2\theta - 1}{2\sqrt{2}} I - \frac{3\sin^2\theta}{2\sqrt{2}} Q\right]. \end{aligned} \tag{4.23b}$$

Noting the radiation field in terms of their irreducible tensor elements provides for an easy link to the molecular states formulated as irreducible tensor elements (see section 3.3). The irreducible tensor elements of molecular states are denoted as, $\rho^k_q(j_i)$, where k is the irreducible tensor element and q its projection, i refers to either the upper maser state a or the lower state b. We consider the case of a strong magnetic field, so that $\rho^k_q(j_i) = 0$ if $q \neq 0$, and we keep ourselves to a $j_a = 1 \rightarrow j_b = 0$ transition. In this case, the lower state, b, cannot be aligned and only has isotropic elements of $k = 0$, while the upper state, a, has an isotropic element of $k = 0$ and an alignment element of $k = 2$.

In order for polarized emission to emerge, we require the maser states to be partially aligned. Because of the condition of a strong magnetic field, this alignment is either parallel or perpendicular to the magnetic field direction, and therefore, polarization is generated either parallel or perpendicular to the magnetic field direction, projected onto the plane of the sky. If we intend to model the emergent maser polarization fraction, it is incumbent to model the relative alignment of the maser states. Just as in section 4.1 on the relative populations of molecular states, we model the relative alignment of the maser states through analyzing the rates of excitation and de-excitation to and from the states of interest. Since we are speaking about a maser, we are mostly interested in the absorption and stimulated emission events between the maser states. We follow the relative alignment of the $j_a = 1$ maser state, $\rho^2_0(j_a)$: the rate of change of this state is

$$\begin{aligned}\dot{\rho}^2_0(j_a) &= -B_{ab}\left[J^2_0\rho^0_0(j_a) + J^0_0\rho^2_0(j_a)\right] + \frac{1}{\sqrt{3}} B_{ba}\bar{J}^2_0\rho^0_0(j_b) - \gamma\rho^2_0(j_a) \\ &= 0, \end{aligned} \tag{4.24}$$

where γ is the maser decay rate (see Eq. (4.16)). We divide Eq. (4.24) by $B_{ab}J_0^0$ and rearrange to obtain an expression for the relative alignment of the $j_a = 1$ maser state

$$\rho_0^2(j_a = 1) = -\frac{\delta_0^2}{\sqrt{3}} \frac{\Delta n}{1 + \frac{J_{\rm sat}}{2\bar{J}_{ab}}}, \tag{4.25}$$

where $\Delta n = n_a - 3n_b = \sqrt{3}[\rho_0^0(j_a) - \sqrt{3}\rho_0^0(j_b)]$ and we have defined the relative anisotropy of the radiation field

$$\delta_0^2 = \frac{\bar{J}_0^2}{\bar{J}_0^0} = \left[\frac{3\cos^2\theta - 1}{2\sqrt{2}} - \frac{3\sin^2\theta}{2\sqrt{2}} \frac{Q}{I} \right]. \tag{4.26}$$

It is interesting to note that in case of an unsaturated maser, $J_{\rm sat} \gg \bar{J}_{ab}$, then the relative alignment of the maser state is absent: $\rho_0^2(j_a = 1) \to 0$. Only in saturated masers, where $\bar{J}_{ab}$ is on the order of, or greater than, the saturation intensity will the radiation field be able to partially align the maser states. In the limit of a highly saturated maser, the alignment of the $j_a = 1$ tends to

$$\rho_0^2(j_a = 1) \simeq -\frac{\delta_0^2}{\sqrt{3}} \Delta n. \tag{4.27}$$

We proceed our analysis and keep ourselves to the highly saturated maser regime. When we do not consider polarization, the line-opacity is given by (see Eq. (4.4))

$$\kappa_\nu = \frac{h\nu}{4\pi} B_{ab} \Delta n \phi_\nu. \tag{4.28}$$

But when the emitting entity is partially aligned, the opacity expressions have to be augmented; and also pertain to the radiation polarization

$$\kappa_I/\kappa_\nu = 1 + \sqrt{3} \frac{\rho_0^2(j_a = 1)}{\Delta n} \frac{3\cos^2\theta - 1}{2\sqrt{2}}, \tag{4.29a}$$

$$\kappa_Q/\kappa_\nu = \sqrt{3} \frac{\rho_0^2(j_a = 1)}{\Delta n} \frac{3\sin^2\theta}{2\sqrt{2}}. \tag{4.29b}$$

We can fill in our expression for the relative alignment of the maser state from Eq. (4.27), and find that the polarized opacity

$$\kappa_Q/\kappa_\nu = -\delta_0^2 \frac{3\sin^2\theta}{2\sqrt{2}}, \tag{4.30}$$

depends only on the relative alignment of the radiation field (Eq. 4.26) and the maser propagation angle θ. In order for the polarization fraction to converge, we require $\kappa_Q \to 0$, which puts a constraint on the polarization fraction

$$\frac{Q}{I} = -\frac{3\sin^2\theta - 2}{3\sin^2\theta}.$$

This polarization fraction is unphysical for $\sin^2\theta < 1/3$ since $|Q/I| > 1$. Under these circumstances, polarization is produced until $|Q/I| \to 1$. We thus have the polarization fraction of a highly saturated maser in the strong magnetic field limit ($\Delta\omega \gg g\Omega \gg R \gg \gamma$):

$$\frac{Q}{I} = \begin{cases} -\frac{3\sin^2\theta - 2}{3\sin^2\theta}, & \text{for } \sin^2\theta \geq \frac{1}{3} \\ 1, & \text{for } \sin^2\theta < \frac{1}{3}, \end{cases} \tag{4.31}$$

which is the classic result of Goldreich et al. (1973).

4.3 Goldreich-Kylafis effect

In previous sections, we discussed excitation modeling within the (isotropic) large-velocity gradient approximation and the alignment of molecular quantum states via directional radiation in masers. Goldreich & Kylafis (1981) combined both these features when considering the (polarized) excitation modeling of a system with an anisotropic large velocity gradient. In this section, we summarize the main physical arguments that lead to the so-called Goldreich-Kylafis (GK) effect.

In section 4.1, we considered the large velocity gradient approximation to solve the radiative transfer and molecular excitation analysis of a non-LTE system. In that discussion, we considered the velocity gradient to be isotropic, but in this section, we consider the more general case of anisotropic velocity gradient. An anisotropic geometry results in an anisotropic radiation field; in section 3.2.2, we showed that anisotropic radiative excitation differentially excites magnetic sublevels, thus leading to the partial alignment of the molecular states.

Because we expect alignment in the molecular states, it cannot be excluded that the radiation is partially polarized. Thus, we need to employ a complete description of the relevant radiation field by including also its partial polarization. We follow Goldreich & Kylafis (1981), and represent the radiation field in terms of their parallel and perpendicular polarized components

$$I_{\parallel,\perp}(\nu,\Omega) = \frac{1}{2}\left(I(\nu,\Omega) \pm Q(\nu,\Omega)\right), \tag{4.32}$$

where the components are with reference to the magnetic field projection on the plane of the sky. We consider a transition between ground state level $j = 0$, and an excited state $j = 1$. In Eqs.(3.42), we computed the radiative interaction rates of absorption transitions $|00\rangle \to |10\rangle$ and $|00\rangle \to |1\pm\rangle$ to be

$$R_0 = B_{01} \int d\nu\ \phi_\nu \int \frac{d\Omega}{4\pi}\ \sin^2\theta I_\parallel(\nu,\Omega), \tag{4.33a}$$

$$R_\pm = \frac{B_{01}}{2} \int d\nu\ \phi_\nu \int \frac{d\Omega}{4\pi} \left(I_\perp(\nu,\Omega) + I_\parallel(\nu,\Omega)\cos^2\theta\right). \tag{4.33b}$$

We use these radiative rates to formulate the rate equations of the populations of the excited state magnetic sublevels n_0 and $n_\pm$, to be

$$\dot{n}_0 = -A_{10}n_0 + R_0(n_g - n_0) + C(n_b e^{-h\nu_0/kT} - n_0), \tag{4.34a}$$

$$\dot{n_\pm} = -A_{10}n_\pm + R_\pm(n_g - n_\pm) + C(n_b e^{-h\nu_0/kT} - n_\pm), \tag{4.34b}$$

$$2n_\pm + n_0 + n_g = \text{constant}, \tag{4.34c}$$

We formulated these equations in terms of $I_{\parallel,\perp}$, instead of the Stokes parameters, because in the case of a constant magnetic field, the radiative transfer of these components can be solved independent from each other.

Because of the anisotropic velocity gradient, the Sobolev length, $s_0(\Omega)$, is in turn a function of the direction. By using the LVG approximation, the profile averaged specific intensity can be solved. Following the same procedure as we did leading up to Eq. (4.13), we obtain

$$\int \frac{d\Omega}{4\pi} \int d\nu \phi_\nu I_{\parallel,\perp}(\nu,\Omega) = \int \frac{d\Omega}{4\pi} \left[S_{\parallel,\perp}(\Omega) - (S_{\parallel,\perp}(\Omega) - \frac{1}{2}I^{(0)}) \frac{1 - e^{-\tau_{\parallel,\perp}(\Omega)}}{\tau_{\parallel,\perp}(\Omega)} \right], \tag{4.35a}$$

where

$$\tau_{\parallel,\perp}(\Omega) = \left(\frac{c}{\nu_0}\right) \frac{s_0(\Omega)}{b} k_{\parallel,\perp}(\Omega). \tag{4.35b}$$

If we adopt for the geometry of the velocity gradient a plane parallel slab, where the magnetic field is oriented along the velocity-gradient, dv/ds. We note that the Sobolev length is,

$$s_0(\Omega) = \frac{b}{dv_{\hat{\boldsymbol{r}}}/dv} = \frac{b}{dv/ds\cos^2\theta} = s_0/\cos^2\theta,$$

where $\cos\theta$ is the projection of the ray-tracing direction on the magnetic field axis. If the velocity gradient is in the directions perpendicular to the magnetic field: $s_0(\Omega) = s_0/\sin^2\theta$. For completeness, the direction dependent propagation coefficients and source functions can be derived to be

$$k_\parallel = \frac{h\nu_0}{4\pi} B_{01}(n_b - n_\pm\cos^2\theta - n_0\sin^2\theta), \tag{4.36a}$$

$$k_\perp = \frac{h\nu_0}{4\pi} B_{01}(n_b - n_\pm), \tag{4.36b}$$

$$S_\parallel = \frac{h\nu_0^3}{c^2} \frac{n_\pm\cos^2\theta + n_0\sin^2\theta}{n_b - n_\pm\cos^2\theta - n_0\sin^2\theta}, \tag{4.36c}$$

$$S_\perp = \frac{h\nu_0^3}{c^2} \frac{n_b - n_\pm}{n_b - n_\pm}. \tag{4.36d}$$

With Eqs.(4.34-4.36), we have obtained a set of equations that can be solved through root-finding methods such as the Newton-Rhapson method. These equations have been first formulated and solved by Goldreich & Kylafis (1981). They yield the polarization fraction as a function of the ratio of radiative to collisional interactions, captured in A_{10}/C, and the average optical depth, τ. For $\tau \sim 1$, polarization fractions are greatest, because at these optical depths, anisotropy in the radiation field best manifests itself. Also, high collisional rates tend to quench the polarization, as the isotropic collisional term in the rate equations de-polarizes the molecular states. In Fig. (4.1) we plot the predicted polarization fraction by the GK model for different ratios A_{10}/C and a range of optical depths. In the same figure, we plot the predicted polarization fractions in case of an unpolarized, but anisotropic radiation field. At low polarization fractions, the two methods converge. This will prove an important insight when modeling the polarization and alignment of radiation and molecular states in more complex geometries, while also including the extensive modeling of a large portion of the rotation-vibration energy-levels of a particular molecule.

4.4 Polarization in a complex geometry

With ever increasing computational power, the comprehensive excitation analysis of molecules in complex astrophysical systems has become viable. We discuss the numerical schemes that allow for the excitation modeling of complex systems. Because the full (polarized) radiative transfer analysis of such systems is still prohibitively complex, we discuss the anisotropic intensity approximation that allows for the polarized excitation analysis of molecular quantum states in a complex geometry, while using the converged output of regular isotropic excitation modeling of these systems.

Up to now, we have discussed radiative transfer and molecular excitation problems in idealized geometries. For maser radiative transfer, we assumed the beaming angle so small that approximating it as one-dimensional propagation is warranted, while for regular molecular excitation, we only discussed the case of geometries with a large (and constant) velocity gradients. The large velocity gradient was invoked so that we could approximate the molecular excitation as being constant in the region, while the constant velocity gradient allowed us to simplify the radiative transfer considerably, and set up a set of coupled equations that can be solved via a root-finding algorithm.

The approximations of one-dimensional propagation or LVG lose their quality when studying astrophysical objects with complex geometries, such as evolved stellar envelopes or protoplanetary disks. Further, with the advent of large interferometers, such objects have been resolved to AU scales, and the interpretation

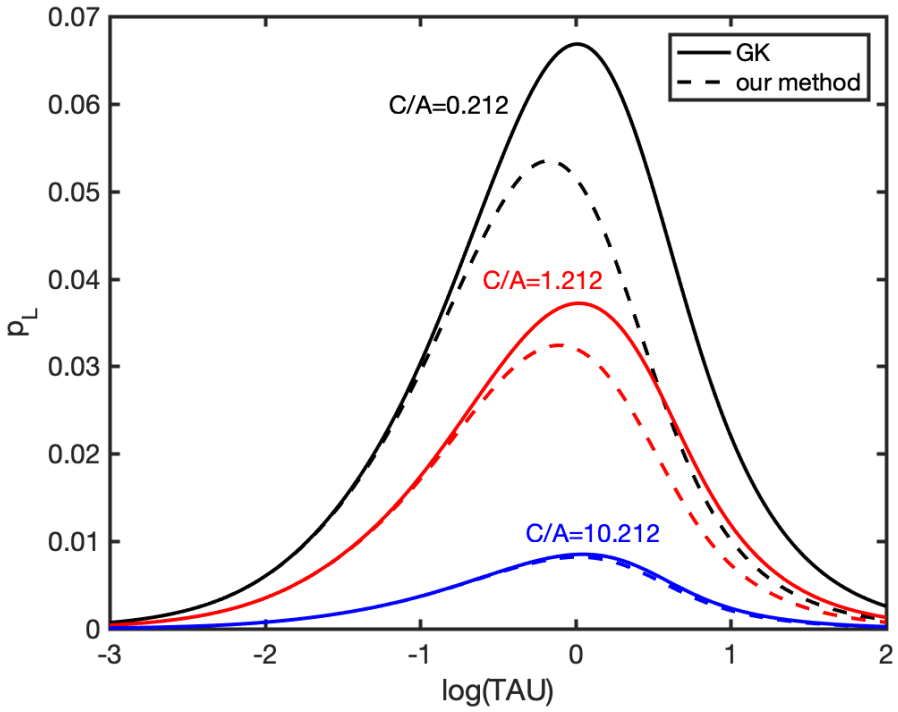

Figure 4.1: Comparison of the polarization fraction computed through the GK method (solid line) and through the radiation anisotropy approximation (dotted line). For more details on the simulation parameters, see Goldreich & Kylafis (1981). We consider a $J = 1 - 0$ transition at 100 GHz, with a strong magnetic field along the $\hat{z}$-axis and a velocity gradient of 10^{-9} s^{-1} in the xy-plane. We consider a temperature $T = 10$ K. Three ratios for the collision-radiative rates are considered and denoted inside the figure. The polarization fraction is computed for a ray traveling along the $\hat{x}$-axis.

of molecular emission from these regions cannot be reasonably interpreted using simplified molecular excitation schemes. Indeed, in the last decades, large improvements have been made in non-local non-LTE analyses of the excitation of molecular lines in complex geometries.

In the numerical work presented in this thesis, when analyzing the non-local (isotropic) molecular excitation in complex geometries, we use the LIne Modeling Engine (LIME), developed by Brinch & Hogerheijde (2010). LIME treats the radiative transfer in a complex geometry that is defined by a density, temperature, velocity and abundance structure. The region is studied, by dividing it up in a (large) number of randomly distributed cells, where the random distribution is density-weighed. The cells are connected by performing a Delaunay triangulation, from which the Voronoi diagram define the cells that are neighboring and connected. The radiative transfer equations are solved, together with the molecular excitation, in a Monte-Carlo scheme, that is sped-up by the Accelerated Lambda Iteration algorithm (Rybicki & Hummer 1991).

Typical numbers of grid-cells for LIME are 100.000, while the molecular excitation per cell includes about 40 rotational levels. Molecules with hyperfine structure, low-lying vibrational levels, or asymmetric rotors require a drastically increased dimensionality of the energy-structure to enable a proper excitation analysis. Thus, the dimensionality of the global excitation analysis is high even without paying attention to molecular alignment and polarized radiation. In paper III, we outline how a polarized excitation analysis can be attained at reasonable computational cost anyway, using two main approximations: (i) the anisotropic intensity approximation, and (ii) the strong magnetic field approximation.

We have seen in our discussion of the polarization of maser radiation, that the relative anisotropy of the radiation field, that quantifies the partial alignment of molecular states due to radiative interactions, is (for one-dimensional propagation)

$$\delta_0^2 = \frac{\bar{J}_0^2}{\bar{J}_0^0} = \left[\frac{3\cos^2\theta - 1}{2\sqrt{2}} - \frac{3\sin^2\theta}{2\sqrt{2}} \frac{Q}{I} \right], \tag{4.37}$$

and has a part that is dependent on the polarization fraction of the radiation field, $p_l = Q/I$. However, from both earlier modeling of GK effects (see Fig. (4.1)), and linear polarization observations of thermal lines, we know that polarization fractions rarely exceed magnitudes of a couple of percents. At these low polarization fractions, it is safe to ignore the contribution of the polarized emission to the anisotropy of the radiation field, and we formulate the radiation field irreducible tensor elements within the anisotropic intensity approximation as

$$\bar{J}_0^0 = \int d\nu \ \phi_\nu \int d\Omega \ I(\nu, \Omega), \tag{4.38a}$$

$$\bar{J}_0^2 = \int d\nu \ \phi_\nu \int d\Omega \ \frac{3\cos^2\theta - 1}{2\sqrt{2}} I(\nu, \Omega). \tag{4.38b}$$

If we use this approximation for obtaining the irreducible tensor elements of the radiation field, they can be obtained for a complex three-dimensional geometry from the solution of a radiative transfer engine such as LIME. Having acquired the irreducible tensor elements of the radiation field at every transition, the relative alignment of the molecular states can be computed and used to ray-trace a polarized image of the region of interest. This is the method we employ in PORTAL, which we present in Paper III, and use to analyze the emergence of polarization from different molecular lines in protoplanetary disks in Paper V.

Bibliography

Ade, P., Aghanim, N., Alina, D., et al. 2015, Astron. Astrophys., 576, A104

Alfvén, H. 1942, Nature, 150, 405

Alfvén, H. 1963, Cosmical electrodynamics (CreateSpace Independent Publishing Platform)

Balbus, S. A. & Hawley, J. F. 1991, Astrophys. J., 376, 214

Balick, B. & Frank, A. 2002, Annu. Rev. Astron. Astrophys., 40, 439

Bartlett, R. J. & Musiał, M. 2007, Rev. Mod. Phys., 79, 291

Beck, R. 2016, Astron. Astrophys. Rev., 24, 4

Berdyugina, S. V. 2008, Proceedings of the International Astronomical Union, 4, 323

Bjerkeli, P., van der Wiel, M. H., Harsono, D., Ramsey, J. P., & Jørgensen, J. K. 2016, Nature, 540, 406

Blandford, R. & Payne, D. 1982, Mon. Not. R. Astron. Soc., 199, 883

Blum, K. 1981, Density Matrix Theory and Applications, Physics of atoms and molecules (New York: Plenum)

Born, M. & Oppenheimer, R. 1927, Annalen der physik, 389, 457

Braithwaite, J. & Spruit, H. C. 2004, Nature, 431, 819

Brinch, C. & Hogerheijde, M. 2010, Astron. Astrophys., 523, A25

Brink, D. M. & Satchler, G. R. 1993, Angular Momentum, 3rd edn. (Oxford: Clarendon)

Brown, J. M. & Carrington, A. 2003, Rotational spectroscopy of diatomic molecules (Cambridge University Press)

Chandrasekhar, S. 2013, Radiative transfer (Courier Corporation)

Chandrasekhar, S. & Fermi, E. 1953, Astrophys. J., 118, 113

Choudhuri, A. R. 1998, The physics of fluids and plasmas: an introduction for astrophysicists (Cambridge University Press)

Chuss, D. T., Andersson, B., Bally, J., et al. 2019, Astrophys. J., 872, 187

Cotton, W., Mennesson, B., Diamond, P., et al. 2004, Astron. Astrophys., 414, 275

Crutcher, R. M. 2012, Annu. Rev. Astron. Astrophys., 50, 29

Crutcher, R. M. & Kemball, A. J. 2019, Front. Astron. Space Sci., 6, 66

Crutcher, R. M., Wandelt, B., Heiles, C., Falgarone, E., & Troland, T. H. 2010, Astrophys. J., 725, 466

Davis Jr, L. & Greenstein, J. L. 1951, Astrophys. J., 114, 206

Degl'Innocenti, M. L. & Landolfi, M. 2006, Polarization in spectral lines, Vol. 307 (Springer Science & Business Media)

Deguchi, S. & Watson, W. D. 1990, Astrophys. J., 354, 649

Dicke, R. H. 1954, Phys. Rev., 93, 99

Draine, B. T. 2010, Physics of the interstellar and intergalactic medium (Princeton University Press)

Eckart, C. 1935, Phys. Rev., 47, 552

Elitzur, M. 1992, Annu. Rev. Astron. Astrophys., 30, 75

Elmegreen, B. G. & Scalo, J. 2004, Annu. Rev. Astron. Astrophys., 42, 211

Falceta-Gonçalves, D. & Jatenco-Pereira, V. 2002, Astrophys. J., 576, 976

Flygare, W. 1978, Molecular Structure and Dynamics (Englewood Cliffs: Prentice-Hall)

Gail, H.-P. & Sedlmayr, E. 2014, Physics and chemistry of circumstellar dust shells, Vol. 52 (Cambridge University Press)

Goldreich, P., Keeley, D. A., & Kwan, J. Y. 1973, Astrophys. J., 179, 111

Goldreich, P. & Kylafis, N. D. 1981, Astrophys. J., 243, L75

Gray, M. 2012, Maser Sources in Astrophysics, Vol. 50 (Cambridge University Press)

Habing, H. J. & Olofsson, H. 2013, Asymptotic giant branch stars (Springer Science & Business Media)

Helgaker, T., Jorgensen, P., & Olsen, J. 2014, Molecular electronic-structure theory (John Wiley & Sons)

Houde, M., Vaillancourt, J. E., Hildebrand, R. H., Chitsazzadeh, S., & Kirby, L. 2009, Astrophys. J., 706, 1504

Hull, C. L. & Zhang, Q. 2019, Front. Astron. Space Sci., 6, 3

Jackson, J. D. 1998, Classical electrodynamics, 3rd edn. (New York: Wiley)

Jeans, J. H. 1902, Phil. T. R. Soc. A, 199, 1

Kataoka, A., Muto, T., Momose, M., et al. 2015, Astrophys. J., 809, 78

Kataoka, A., Tsukagoshi, T., Pohl, A., et al. 2017, Astrophys. J. Lett., 844, L5

Klemperer, W., Lehmann, K., Watson, J., & Wofsy, S. 1993, J. Phys. Chem., 97, 2413

Krumholz, M. R. 2015, arXiv, arXiv

Krumholz, M. R. & Federrath, C. 2019, Front. Astron. Space Sci., 6, 7

Kulsrud, R. M. 2020, Plasma physics for astrophysics (Princeton University Press)

Kunz, M. W. & Mouschovias, T. C. 2009, Astrophys. J., 693, 1895

Kwok, S., Purton, C. R., & Fitzgerald, P. M. 1978, Astrophys. J., 219, L125

Lamers, H. J., Cassinelli, J. P., & Cassinelli, J. 1999, Introduction to stellar winds (Cambridge university press)

Landau, L. D., Lifshitz, E. M., & Pitaevskii, L. 1980, Statistical physics: theory of the condensed state, Vol. 9 (Butterworth-Heinemann)

Lazarian, A. & Hoang, T. 2007, Mon. Not. R. Astron. Soc., 378, 910

Lazarian, A. & Vishniac, E. T. 1999, Astrophys. J., 517, 700

Lin, C. C. & Swalen, J. D. 1959, Rev. Mod. Phys., 31, 841

Morris, M., Lucas, R., & Omont, A. 1985, Astron. Astrophys., 142, 107

Moss, R. & Perry, A. 1973, Mol. Phys., 25, 1121

Mouschovias, T. C. & Ciolek, G. E. 1999, in The Origin of Stars and Planetary Systems (Springer), 305–340

Nordhaus, J., Blackman, E., & Frank, A. 2007, Mon. Not. R. Astron. Soc., 376, 599

Ossenkopf, V. 1997, New Astron., 2, 365

Papousek, D. & Aliev, M. R. 1982

Parker, E. N. 1955, Astrophys. J., 122, 293

Parker, E. N. 1957, J. Geophys. Res., 62, 509

Parker, E. N. 2019, Cosmical magnetic fields: Their origin and their activity (Oxford Classic Texts in the Ph)

Podolsky, B. 1928, Phys. Rev., 32, 812

Pringle, J. 1981, Annu. Rev. Astron. Astrophys., 19, 137

Racah, G. 1942, Phys. Rev., 62, 438

Rajabi, F. & Houde, M. 2020, Mon. Not. R. Astron. Soc., 494, 5194

Roothaan, C. C. J. 1951, Rev. Mod. Phys., 23, 69

Rudnitski, G., Pashchenko, M., & Colom, P. 2010, Astron. rep., 54, 400

Rybicki, G. B. & Hummer, D. G. 1991, Astron. Astrophys., 245, 171

Rybicki, G. B. & Lightman, A. P. 2008, Radiative processes in astrophysics (John Wiley & Sons)

Sauer, S. P. 2011, Molecular electromagnetism: a computational chemistry approach (OUP Oxford)

Semel, M. 1989, Astron. Astrophys., 225, 456

Shu, F. H. 1977, Astrophys. J., 214, 488

Shu, F. H. 1991a, The Physics of Astrophysics: Gas Dynamics, Vol. 2 (University Science Books)

Shu, F. H. 1991b, The Physics of Astrophysics: Radiation, Vol. 1 (University Science Books)

Shu, F. H., Najita, J. R., Shang, H., & Li, Z.-Y. 2000, Protostars and Planets IV, 789, 31

Sobolev, V. 1957, Sov. Astron., 1, 678

Soker, N. 1998, Mon. Not. R. Astron. Soc., 299, 1242

Stephens, I. W., Yang, H., Li, Z.-Y., et al. 2017, Astrophys. J., 851, 55

Szabo, A. & Ostlund, N. S. 2012, Modern quantum chemistry: introduction to advanced electronic structure theory (Courier Corporation)

Tan, J. C., Beltrán, M. T., Caselli, P., et al. 2014, Protostars and Planets VI, 149

Thorne, K. S. & Blandford, R. D. 2017, Modern Classical Physics: Optics, Fluids, Plasmas, Elasticity, Relativity, and Statistical Physics (Princeton University Press)

Trippella, O., Busso, M., Palmerini, S., Maiorca, E., & Nucci, M. 2016, Astrophys. J., 818, 125

van der Tak, F., Black, J. H., Schöier, F., Jansen, D., & van Dishoeck, E. F. 2007, Astron. Astrophys., 468, 627

Van Winckel, H. 2003, Annu. Rev. Astron. Astrophys., 41, 391

Vlemmings, W. 2018, Proceedings of the International Astronomical Union, 14, 19

Vlemmings, W., Torres, R., & Dodson, R. 2011, Astron. Astrophys., 529, A95

Vlemmings, W. H., Diamond, P. J., & Imai, H. 2006, Nature, 440, 58

Vlemmings, W. H. & van Langevelde, H. J. 2005, Astron. Astrophys., 434, 1021

Widrow, L. M. 2002, Rev. Mod. Phys., 74, 775

Wigner, E. P. 1951in , Cambridge University Press, 790–798

Wilson, E. B., Decius, J. C., & Cross, P. C. 1980, Molecular vibrations: the theory of infrared and Raman vibrational spectra (Courier Corporation)

Xu, L.-H. & Lovas, F. 1997, J. Phys. Chem. Ref. Data, 26, 17

Yen, H.-W., Zhao, B., Koch, P. M., et al. 2018, Astron. Astrophys., 615, A58

Zwaan, C. 1987, Annu. Rev. Astron. Astrophys., 25, 83

Acknowledgements

Wouter Vlemmings supervised the work that is presented in this thesis. He took a risk when taking me in as a PhD student in his group, considering my unusual background in the field of astronomy. Our discussions and collaboration have been very fruitful to me, and I think the work in this thesis is all the better for it. I have been continually impressed by his ability to quickly understand complex problems. Wouter's willingness to let me free and find my own path through the field, while supporting my efforts with insightful guidance, has lead to a thesis that I hope is an original approach to some problems in Astrophysics.

I would also like to thank the supervisors of my work as a MSc student at the Radboud University, Gerrit Groenenboom and Ad van der Avoird. They have contributed greatly to the work in Paper I. In particular, Ad van der Avoird has always been very generous with his time and extraordinary prompt and thorough with his criticism. Both Ad and Gerrit have taught me to be critical in ways that I could not have conceived of my own.

The administrative staff of both the Onsala Space Observatory, Paula and Pia, and of the Astronomy & Plasma physics division, Paulina and Robin, have been very helpful in navigating all of those things that happen behind the scenes of science. Apart from their help, they have also been great in keeping up morale with enthusiasm and lightheartedness at coffee breaks.

The students, postdocs and faculty of AoP and SEE together take care of a great atmosphere to work in. For that reason, Chalmers is a very agreeable place to work at. Beyond that, it has also lead to some very interesting collaborations which have not been included in this thesis.

My Fiancée, Yasmin, cheered me up and kept me disciplined. She has been there for me always, and has put up with my occasional moodiness. I look forward to our future. My family has always supported my ambitions and I cherish the warm relationship we have. I hope I will have the opportunity ot one day reward their faith and support.